

Run Group Proposal with E12-12-006 at Jefferson Lab PAC 43
Timelike Compton Scattering on the proton
in e^+e^- pair production with SoLID at 11 GeV

I. Albayrak,¹ A. Camsonne,² M. Boer*,³ D. Crabb,⁴ D. Day,⁴ N. Dien,⁴ M. Guidal,³ V. Guzey,⁵
 T. Horn,¹ C. Hyde,⁶ Y. Ilieva,⁷ D. Keller,⁴ H.-S. Jo,³ C. Keppel,² P.E.C. Markowitz,⁸
 H. Moutarde,⁹ C. Munoz Camacho,³ P. Nadel-Turonski*,² R. Paremuzyan,^{3,10} P. Gueye,¹¹
 B. Pire,¹² F. Sabatié,⁹ P. Schweitzer,¹³ S. Stepanyan,² L. Szymanowski,¹⁴ A. Thomas,¹⁵
 J. Wagner,¹⁴ C. Weiss,² N. Zachariou,⁷ J. Zhang*,⁴ Y. Zhao,¹⁶ and Z.W. Zhao * †¹⁷

¹*Catholic University of America, Washington, D.C. 20064*

²*Thomas Jefferson National Accelerator Facility, Newport News, Virginia 23606*

³*Institut de Physique Nucleaire d'Orsay, IN2P3, BP 1, 91406 Orsay, France*

⁴*University of Virginia, Charlottesville, VA 22904*

⁵*Petersburg Nuclear Physics Institute, Gatchina 188300, Russia*

⁶*Old Dominion University, Norfolk, Virginia 23529*

⁷*University of South Carolina, Columbia, South Carolina 29208*

⁸*Florida International University, Miami, Florida 33199*

⁹*CEA, Centre de Saclay, Irfu/Service de Physique Nucléaire, 91191 Gif-sur-Yvette, France*

¹⁰*Yerevan Physics Institute, 375036 Yerevan, Armenia*

¹¹*Hampton University, Hampton, VA 23668*

¹²*CPhT, École Polytechnique, 91128 Palaiseau, France*

¹³*University of Connecticut, Storrs, Connecticut 06269*

¹⁴*National Center for Nuclear Research (NCBJ), 00-681 Warsaw, Poland*

¹⁵*University of Adelaide, Adelaide SA 5005 AUSTRALIA*

¹⁶*University of Science and Technology of China, Heifei, Anhui 230026, China*

¹⁷*Duke University, Durham, NC 27708*

(Dated: May 18, 2015)

*Co-spokesperson

†Contact person: zwzhao@jlab.org

We propose to measure exclusive e^+e^- production with the SoLID detector using an 11 GeV polarized beam and a LH_2 target to study the reaction $\gamma p \rightarrow \gamma^* p' \rightarrow e^+e^- p'$, known as Timelike Compton Scattering (TCS), which is the timelike equivalent of (spacelike) DVCS. Both the differential cross section, beam-spin asymmetry (BSA) with circularly polarized photons, and moments of the weighted cross section will be measured as a function of the four-momentum transfer $-t$, the outgoing photon virtuality Q'^2 (up to 9 GeV²), and the skewness η . The latter reflects the difference between the initial and final momentum fraction carried by the struck quark, and corresponds to ξ in DVCS. In TCS, the BSA with circularly polarized photons is sensitive to the imaginary part of the Compton form factors (CFFs), while the unpolarized cross section is primarily sensitive to the real part. With circularly polarized photons, the weighted moments can be sensitive to both. A comparison with DVCS can test the universality of GPDs, while a combined fit to both DVCS and TCS observables can reduce the uncertainty on the measured CFFs, making the two processes complementary. The high luminosity of SoLID will make it possible to perform a mapping of the Q'^2 - and η -dependence, which is essential for understanding factorization, higher-twist effects, and NLO corrections. It is also of particular importance for global fits aimed at extracting GPDs. This proposed experiment is complementary to the approved CLAS12 experiment E12-12-001 [1], which will measure the t -dependence in wider bins of Q'^2 and η , with the focus on a first measurement of the so-called D -term. The CLAS12 and SoLID experiments are further mutually supportive in that performing this new kind of measurement using two detector setups, each with a different acceptance, will provide an essential cross check, and could also result in reduced overall systematic uncertainties. The proposed experiment can run in parallel with experiment E12-12-006 [2], which has been approved for 60 days. The projections are thus shown for an effective 50 days of running.

Contents

1. Introduction	4
2. Physics of Timelike Compton Scattering	7
A. Kinematics	7
B. Leading-twist formalism	8
C. TCS cross section and interference between TCS and BH amplitudes	13
D. Cross sections and beam asymmetries	17
1. Decay angular dependencies of the unpolarized cross section	17
2. Circularly polarized beam spin asymmetry	18
E. NLO corrections	19
1. The TCS amplitudes	21
2. Timelike Compton Form Factors	21
3. Cross sections and asymmetries	24
F. Amplitude analysis of Compton form factors	26
G. Comment on dispersion analysis	29
H. Results from CLAS 6 GeV data	29
3. Experimental Setup	32
A. SoLID detector	32
B. Detection of exclusive e^+e^-p events	35
C. Trigger	38
D. Event Distribution	39
4. Projected Results	41
A. Moment approach	42
B. Local fit of Compton form factors approach	44
C. Conclusion	47
5. Systematic Uncertainties	48
6. Running condition	49
References	50

1. INTRODUCTION

Understanding the structure and interactions of hadrons on the basis of Quantum Chromodynamics (QCD) is one of the main objectives of nuclear physics. The combination of fundamental properties of QCD as a quantum field theory, such as relativity and causality, with factorization theorems allows us to systematically explore the partonic structure of hadrons through various processes using different probes. In this context, the correspondence between spacelike and timelike processes plays a unique role.

Let us consider the Drell-Yan process, $h\bar{h} \rightarrow \gamma^* X \rightarrow l\bar{l}X$, where γ^* has a timelike virtuality ($Q^2 > 0$), h (\bar{h}) denotes a baryon (antibaryon), and l (\bar{l}) a lepton (antilepton). This reaction provides important information on (anti)quark distributions in the hadrons h and \bar{h} . The same distributions are, however, also probed in inclusive deep inelastic scattering (DIS), $lh \rightarrow l'X$, mediated by an exchange of a spacelike virtual photon ($Q^2 < 0$), $\gamma^*h \rightarrow X$. A comparison of the Drell-Yan and DIS results thus convincingly demonstrated the universality of parton distribution functions (PDFs). In this proposal we focus on the correspondence between timelike and spacelike deeply virtual Compton scattering (DVCS), where the former is also known as timelike Compton scattering (TCS), and the universality of generalized parton distributions (GPDs), measured in hard exclusive processes.

In the last 15 years, hard exclusive processes have emerged as a class of reactions providing novel information on the quark and gluon distributions in hadrons. This information is more complete than what can be obtained from inclusive and elastic scattering alone; for reviews, see Refs. [3–5]. QCD factorization theorems [6, 7] make it possible to express amplitudes of hard exclusive processes in terms of GPDs, which are expected to provide a universal (process-independent) description of the nucleon, and have a known QCD (Q^2) evolution. GPDs are hybrid distributions that combine aspects of the usual collinear PDFs, elastic form factors, and distribution amplitudes. As such, GPDs simultaneously encode information on parton distributions and correlations in both momentum (in the longitudinal direction) and coordinate (in the transverse direction) spaces. Another interesting aspect of GPDs is their connection to the form factors of the energy-momentum tensor, which, among other things, establishes the decomposition of the proton spin in terms of the quark and gluon contributions to the total orbital momentum [8].

The best studied hard exclusive process is DVCS, $\gamma^*p \rightarrow \gamma p$, where the initial-state virtual photon is spacelike ($Q^2 < 0$), and the final-state photon is real. From a theoretical point of view, it is the simplest and cleanest way to access GPDs. The leading-twist formalism is well established for DVCS at the leading and next-to-leading orders in the strong coupling constant, and power-suppressed corrections have been analyzed and estimated. On the experimental side, early data have demonstrated the feasibility of DVCS measurements, established the reaction

mechanism based on the leading-twist approach (the handbag mechanism), and provided first glimpses of the Compton form factors (CFFs) and the related GPDs. The goal of determining the valence quark GPDs in the nucleon through measurements of DVCS and other hard exclusive processes is now a cornerstone of the 12 GeV program at Jefferson Lab.

Recently, a promising opportunity has emerged for extending our understanding of GPDs by studying the timelike equivalent of traditional, spacelike DVCS. The process, $\gamma p \rightarrow \gamma^* p$, is known as timelike Compton scattering (TCS). Here, the timelike final-state photon immediately decays into a lepton pair, the invariant mass of which is a measure of the photon virtuality ($Q'^2 > 0$), and provides the hard scale for the reaction. The leading-twist formalism for TCS [9] (the factorization theorem, the handbag reaction mechanism, etc) is as well established as that for DVCS. However, as also shown in Ref. [9], the phenomenology of TCS is quite different from DVCS. With an unpolarized photon beam, TCS offers straightforward access to the real part of the CFFs through the interference between the Compton and Bethe-Heitler (BH) amplitudes, which can be extracted in a model-independent way from the azimuthal angular distribution of the lepton pair into which the timelike photon decays. Circular photon polarization also gives access to the imaginary part of CFFs. In summary, the main motivation to study TCS includes:

- A measurement of TCS will make it possible to test the universality of GPDs implied by factorization through the timelike-spacelike correspondence with DVCS.
- The straightforward access in TCS to, in particular, the real part of the CFFs impacts models and parametrizations of GPDs in a broad range of kinematics (light-cone fractions τ and η , which are the equivalent of x and ξ in DVCS).
- The differential cross section (for TCS and its interference with BH) can provide important input for global fits of CFFs [10, 11].

However, a solid interpretation of the results from the TCS program, will also require understanding of higher-twist and NLO corrections (in α_s). A general framework for the calculation of kinematic higher-twist corrections, proportional to $|t|/Q'^2$ and M^2/Q'^2 , has recently been developed for hard exclusive reactions [12]. The formalism was applied to DVCS [13] and it was found the higher twist corrections are important for $Q^2 = 1 - 10 \text{ GeV}^2$, *i.e.*, for the kinematics largely overlapping with that of Jefferson Lab at 6 and 12 GeV. Thus, if one wants to study factorization and effects related to higher-twist contributions, it is crucial to be able to map out the full range in Q'^2 with sufficient statistics for the highest points.

Recent calculations [?] suggest that the NLO corrections may be sizeable, and larger for TCS than DVCS. They are, however, expected to be small at large values of the skewness η (*i.e.*, above values of 0.3-0.4), corresponding to a large difference between the initial and final momentum fraction carried by the struck quark. They then increase rapidly as η approaches

0.1, which is at the lower limit of the reach of 12 GeV kinematics. The expression for η is

$$\eta = -\frac{(q - q') \cdot (q + q')}{(p + p') \cdot (q + q')} = \frac{Q'^2}{2(s - M^2) - Q'^2 + t} = \frac{Q'^2}{4ME_\gamma - Q'^2 + t}, \quad (1)$$

where q , q' , p , and p' are defined in Eq. 2, M is the proton mass, and E_γ is the incident photon energy. As in DVCS, we have that $\eta \approx \tau/(2 - \tau)$, where τ is the TCS equivalent of Bjorken x . Since large values of η naturally correspond to large Q'^2 , doing the mapping in η requires sufficient statistics at high values of Q'^2 , where the cross section is small, and small bins in the transition to lower values of η , where the change in the magnitude of the NLO corrections is expected to be rapid. Thus, in 12 GeV kinematics the region of high Q'^2 , where both higher-twist and NLO corrections are expected to be small, provides a natural reference point. On the other hand, the NLO corrections are almost entirely due to gluons. If they turn out to be significant at lower values of η , and since they are predicted to be larger in TCS than DVCS, TCS could become a very interesting new tool for studying gluons at 12 GeV.

The primary goal of this proposed experiment for SoLID is to make a precision study of the Q'^2 - and η -dependence of the differential cross section and moments of the weighted cross section up to the highest values of Q'^2 , for which the high luminosity of SoLID is essential. This proposal is thus complementary to the approved CLAS12 experiment E12-12-001, which will focus on studying the t -dependence in larger bins of Q'^2 and η . The two detectors also offer complementary capabilities. In particular, the SoLID detector, being based on a solenoidal magnet, has a more uniform acceptance in the azimuthal angle φ than CLAS12, but has a gap in the ϑ -coverage between the inner (forward) and outer detectors. Performing this new kind of measurement using two setups, each with a different acceptance, will not only provide an essential cross check, but could result in reduced overall systematic uncertainties on, for instance, the real part of the Compton form factor \mathcal{H} .

The feasibility of the experimental techniques involved in the measurement, including the use of quasi-real photons (with $Q^2 < 0.1 \text{ GeV}^2$) tagged by detecting the complete final state except for the beam electron, have been demonstrated in the analysis of CLAS 6 GeV data, which include pilot studies of TCS. In terms of experimental requirements, photoproduction measurements in SoLID will require time-of-flight detectors covering both the inner (forward) as well as the outer calorimeter. The trigger for the reaction will have to include at least two leptons and could require an additional track using the time-of-flight rather than Cherenkov detector. We thus propose to measure exclusive e^+e^- production using the SoLID detector and an 11 GeV linearly polarized electron beam and a LH_2 target to study TCS over a wide range of Q'^2 , η , and t . Both the differential cross section and the cosine and sine moments of the weighted cross section will be measured.

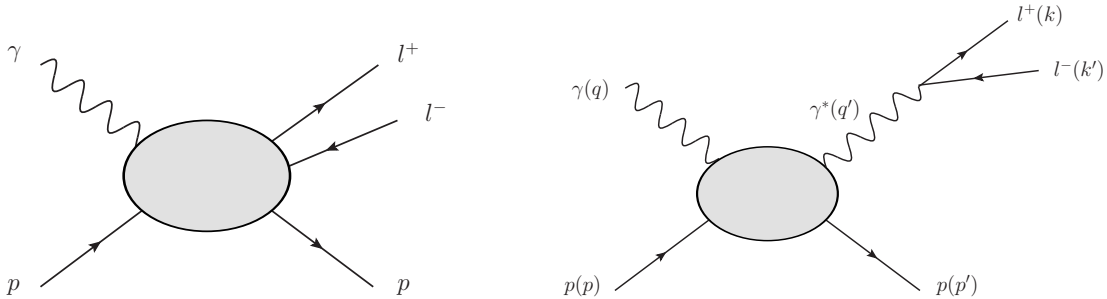


FIG. 1: *Left panel:* Exclusive photoproduction of a lepton pair. *Right panel:* Timelike Compton scattering (TCS). The particle momenta are given in parenthesis.

2. PHYSICS OF TIMELIKE COMPTON SCATTERING

In this section we describe the theory and phenomenology of the timelike Compton process, discuss observables, and present model calculations. We also explain how the data can be used in global fits, and show 6 GeV analysis results.

A. Kinematics

Timelike Compton Scattering (TCS),

$$\gamma(q) + p(p) \rightarrow \gamma^*(q') + p(p'), \quad (2)$$

is the process of photoproduction of a virtual timelike photon ($q'^2 = Q'^2 > 0$) on a nucleon. As shown in the right panel of Fig. 1, the final-state virtual photon immediately decays into a lepton pair. TCS is, however, not the only physical processes that can be observed in exclusive photoproduction of lepton pairs, $\gamma p \rightarrow l^+ l^- p$. Another process with the same final state is the purely electromagnetic Bethe-Heitler (BH) reaction shown in Fig. 2. Like in DVCS, the TCS and BH amplitudes interfere. In JLab 12 GeV kinematics, where the BH cross section is significantly larger than the TCS cross section, one can take advantage of this interference to enhance the TCS signal; see Sect. 2 C for details.

The TCS amplitude depends on the following three kinematic invariants:

$$\begin{aligned} q'^2 &= Q'^2 > 0, \\ s &= (p + q)^2, \\ t &= (p' - p)^2, \end{aligned} \quad (3)$$

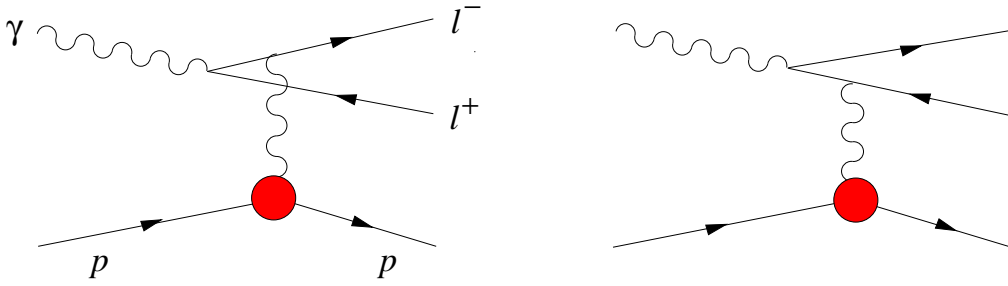


FIG. 2: The Feynman graphs for the Bethe-Heitler contribution to the $\gamma p \rightarrow l^+ l^- p$ process.

where $q'^2 = Q'^2$ is the virtuality of the final-state photon, s is the invariant photon-proton energy squared, and t is the four-momentum transfer squared. In addition to these three variables, the $\gamma p \rightarrow l^+ l^- p$ cross section depends on the angles θ and φ associated with the final-state lepton pair. In the $l^+ l^-$ center-of-mass frame, θ is the angle between the momenta of the lepton \vec{k} and the recoiling proton \vec{q}' , and φ is the angle between the reaction plane and the lepton decay plane, as shown in Fig. 3.

B. Leading-twist formalism

To ensure the applicability of the leading twist formalism to the $\gamma p \rightarrow l^+ l^- p$ process (the left panel of Fig. 1, one requires that (i) the timelike virtuality of the final-state photon, Q'^2 , is sufficiently large to provide a hard scale, (ii) the invariant photon-proton c.m. energy, \sqrt{s} , is sufficiently large to ensure the usual DIS kinematics, and (iii) the invariant momentum transfer squared t is low, *i.e.*, $|t| \leq 1 \text{ GeV}^2$. The timelike nature of the final state also makes interpretation complicated in the presence of resonances in the invariant mass of the produced lepton pair. Hence, as shown in Fig. 4, an ideal mass range for this experiment is $M_{\rho'} < M_{l^+ l^-} < M_{J/\psi}$, which coincides well with JLab 12 GeV kinematics. Since the invariant mass of the lepton pair, $M_{l^+ l^-}$, is also the timelike virtuality of the outgoing photon, Q' , focusing on the resonance-free region automatically satisfies condition (i) above.

The leading-twist formalism for TCS has been developed in Ref. [9]. It is based on the factorization theorem [7] that allows one to express the TCS amplitude in Eq. (2) as convolutions of calculable hard-scattering kernels with GPDs. The resulting quantities are called Compton form factors (CFFs). One expects that as long as Q'^2 is sufficiently large, the leading-twist approximation (*i.e.*, ignoring terms of the order of m_N^2/Q'^2 , m_l^2/Q'^2 , and $|t|/Q'^2$) should work equally well for TCS as it does for DVCS. In other words, one does not expect enhanced higher twist corrections specific to TCS [4].

To leading order in the strong coupling constant, α_s , the TCS amplitude is given by

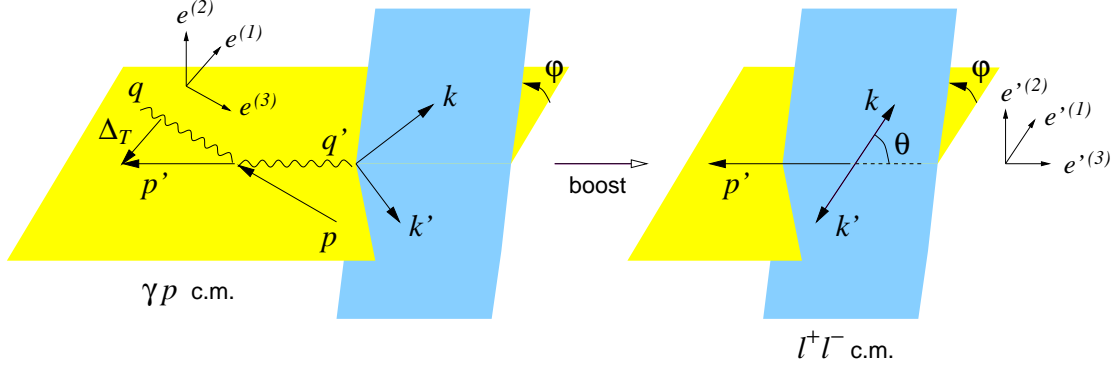


FIG. 3: Momenta and angles involved in the TCS cross section in the γp and $l^+ l^-$ center-of-mass frames. Adopted from [9]. Note that the angles φ and θ will be referred to explicitly as φ_{CM} and θ_{CM} outside of the motivation section to avoid confusion with the angles in the lab system.

the two handbag diagrams presented in Fig. 5. To leading order in α_s , the TCS amplitude is equivalent to the DVCS amplitude, making it easier to test the universality of GPDs. However, at the next-to-leading order, the expressions for the hard scattering kernels for TCS and DVCS are different and, as a result, the TCS and DVCS CFFs have different forms [14, 15]. This is discussed further in Sect. 2E.

The proton has four leading-twist parton-helicity non-flip quark GPDs. The expressions for the corresponding CFFs, \mathcal{H}_1 , \mathcal{E}_1 , $\tilde{\mathcal{H}}_1$, and $\tilde{\mathcal{E}}_1$ are:

$$\begin{aligned}
\mathcal{H}_1(\eta, t) &= \sum_q e_q^2 \int_{-1}^1 \left(\frac{H^q(x, \eta, t)}{\eta - x + i\epsilon} - \frac{H^q(x, \eta, t)}{\eta + x + i\epsilon} \right), \\
\mathcal{E}_1(\eta, t) &= \sum_q e_q^2 \int_{-1}^1 \left(\frac{E^q(x, \eta, t)}{\eta - x + i\epsilon} - \frac{H^q(x, \eta, t)}{\eta + x + i\epsilon} \right), \\
\tilde{\mathcal{H}}_1(\eta, t) &= \sum_q e_q^2 \int_{-1}^1 \left(\frac{\tilde{H}^q(x, \eta, t)}{\eta - x + i\epsilon} + \frac{\tilde{H}^q(x, \eta, t)}{\eta + x + i\epsilon} \right), \\
\tilde{\mathcal{E}}_1(\eta, t) &= \sum_q e_q^2 \int_{-1}^1 \left(\frac{\tilde{E}^q(x, \eta, t)}{\eta - x + i\epsilon} + \frac{\tilde{E}^q(x, \eta, t)}{\eta + x + i\epsilon} \right), \tag{4}
\end{aligned}$$

where the superscript q denotes the quark flavor and e_q the quark charge. For brevity, we suppressed the Q^2 -dependence of the GPDs and CFFs. In Eq. (4), the light-cone fraction η , which in TCS plays the role of the skewness ξ in DVCS, is fixed by the external kinematics:

$$\eta = -\frac{(q - q') \cdot (q + q')}{(p + p') \cdot (q + q')} \approx \frac{Q'^2}{2(s - M^2) - Q'^2 + t}. \tag{5}$$

From Eq. (4) it follows that the imaginary part of the CFFs can be expressed in terms of GPDs along the so-called cross-over line, *i.e.*, at $x = \eta$ for quarks and $x = -\eta$ for antiquarks.

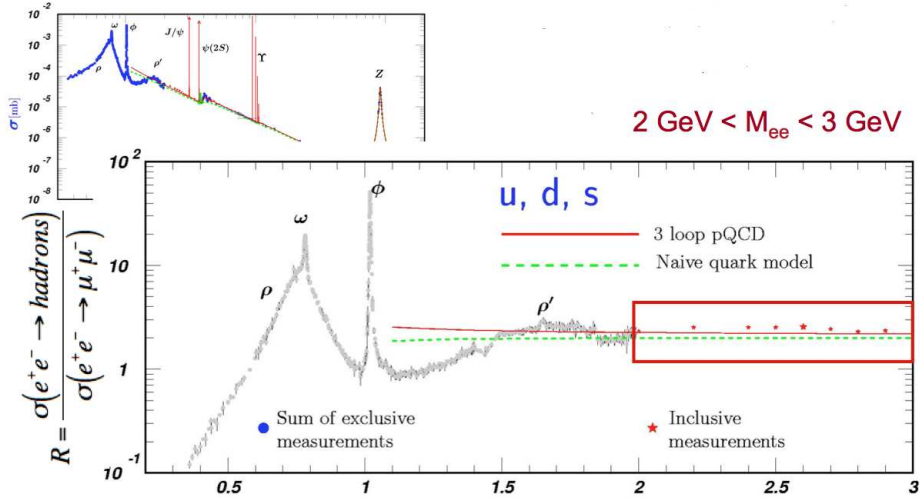


FIG. 4: Measurements of e^+e^- annihilation into hadrons show a resonance-free window between the ρ' and the J/ψ , which is ideal for TCS studies at 12 GeV.

The real part of the CFFs is, on the other hand, sensitive to GPDs over the entire range of x . For instance, the real part of the CFF \mathcal{H}_1 is given by:

$$\Re \mathcal{H}_1(\eta, t) = \sum_q e_q^2 p.v. \int_{-1}^1 \left(\frac{H^q(x, \eta, t)}{\eta - x} - \frac{H^q(x, \eta, t)}{\eta + x} \right), \quad (6)$$

where $p.v.$ stands for the principal value. The straightforward access to the real part of CFFs (see Sect. 2 C) gives TCS measurements the potential to constrain GPDs away from the cross-over line in a wide range of x and η .

The imaginary part of the Compton amplitude is now relatively well understood, primarily through measurements of DVCS – see, *e.g.*, [10]. However, much less is known about the real part, which may become important at larger values of x , coinciding with JLab 12 GeV kinematics. The limited knowledge of the real part of the amplitude is reflected in GPD model predictions, which are in good general agreement for the imaginary part, but differ significantly when it comes to the real one. This is illustrated in Figs. 6 and 7, which show the real and imaginary parts of the GPD H as a function of x and $-t$, respectively, for two GPD models: the dual parametrization [16–19] and the double distribution [20]. The potential of TCS to provide additional constraints on the real part of CFFs is thus important for developing more accurate GPD models. The TCS data could also be used in global fits of CFFs and for dispersion relation analysis. This is discussed in more detail in Sect. 2 F and Sect. 2 G, respectively.

In TCS, the use of a circularly polarized photons allows to determinate both the real and imaginary parts of the helicity amplitudes or CFFs with comparable uncertainties. In contrast, DVCS measurements strongly favor the imaginary part. The real part is only available

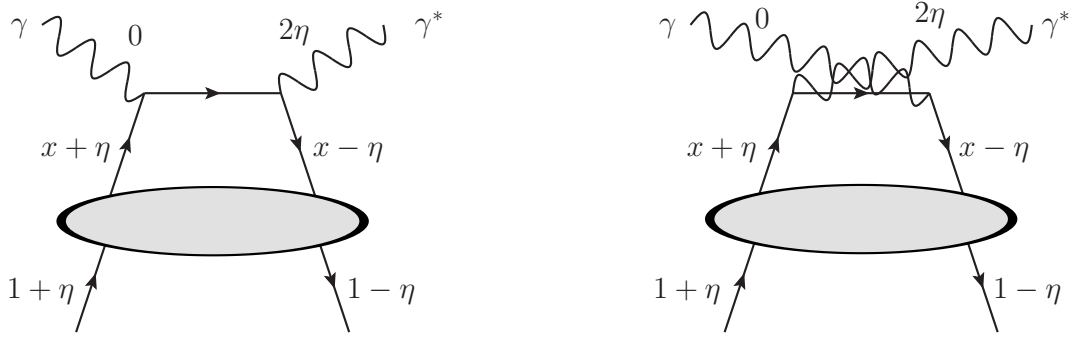


FIG. 5: The handbag diagrams for TCS. The plus-momentum fractions refer to the average proton momentum $(p + p')/2$.

through direct cross section measurements or comparisons of cross sections measured with electron and positron beams, both of which are significantly more challenging than, for instance, the measurement of beam spin asymmetries that give access to the imaginary part.

In addition to discriminating between GPD models and constraining fits of CFFs, a measurement of TCS may also offer a unique possibility to address the issue of the so-called D -term [21]. Technically, the D -term is defined as the contribution to the GPD H and E that provides the highest power of ξ in Mellin moments of this GPD. The D -term of the GPD E has the same magnitude but opposite sign. The D -term contribution to GPDs has support only in the region $x \in [-\eta, \eta]$, which makes it elusive and inaccessible in the forward limit. This unambiguously indicates that the D -term cannot be interpreted in terms of the usual parton densities. Instead, the D -term describes the emission of a $q\bar{q}$ pair by the nucleon, revealing the complex nature of the nucleon as a many-body system.

The D -term [21] was originally introduced in the context of the double distribution (DD) parametrization of GPDs [20], as an additional function required to generate the highest $n + 1$ power of x_i in the x^n moment of the GPD $H(x, x_i)$. It was realized [22] that the same result could be achieved within a single-DD parameterization (*i.e.*, one using only the forward parton distributions as input), but at the price of introducing singular expressions requiring additional prescriptions. Because of the need to deal with singular functions this method was not widely used for modeling GPDs. However, a recent theoretical analysis of the single-DD parametrization [23] demonstrated explicitly how all arising singular expressions can be regularized and how the D -term naturally appears in this approach, so that the relation between the two parametrizations is now well understood. Coupled with the imbedded Regge formalism, the single-DD parametrization thus offers a new alternative approach to modeling GPDs.

The distribution of energy, momentum, and angular momentum in the nucleon is charac-

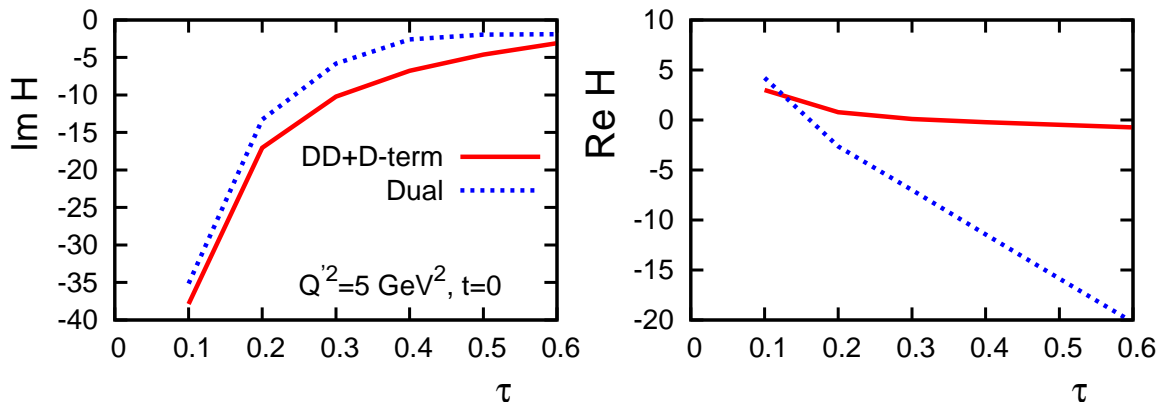


FIG. 6: Imaginary (left) and real (right) parts of the GPD H plotted as a function of $\tau = Q'^2/(s - M^2)$, which is the TCS equivalent of Bjorken x , for $Q'^2 = 5 \text{ GeV}^2$ and $t = 0$. The curves correspond to GPD models based on the dual parametrization [16–19] and the double distribution [20], respectively.

terized by form factors of the QCD energy-momentum tensor between the nucleon states [8, 24], all of which can be expressed in terms of GPDs. The D -term gives rise to one of these form factors (denoted $C(t)$ or $d_1(t)$ in the literature).

It has been shown that in the Breit frame, this form factor can be interpreted as describing the distribution of pressure and shear forces acting on quarks inside the nucleon [25]. Studies in field-theoretical models show that the negative sign of the D -term is a consequence of the stability of the nucleon [26]. This is illustrated in Fig. 9, where the pressure $p(r)$ experienced by quarks inside the nucleon is given as a function of the distance from the center, r . Stability arises as a balance between repulsive forces in the inner region, and attractive forces at large r , such that the stability condition $\int_0^\infty dr r^2 p(r) = 0$ holds. The D -term is given by $d_1 = 5\pi M \int_0^\infty dr r^4 p(r)$ and the additional weight r^2 in the integrand emphasizes the role of large distances and binding forces inside the nucleon, leading to a negative value of the D -term [26].

Form factors of the QCD energy-momentum tensor can also be calculated from first principles in lattice QCD. The QCDSF collaboration calculated the D -term form factor $d_1(t)$ as a function of $-t$ for the pion mass $m_\pi = 640 \text{ MeV}$ [27]. The predictions of the chiral quark-soliton model [26] used for the calculation shown in Fig. 9 are in agreement with the lattice data.

The notion of the D -term is important for phenomenology because it (i) is an integral ingredient of GPD modeling (see the discussion above), (ii) gives an energy-independent (η -independent) contribution to $\Re H_1$ and $\Re E_1$, and (iii) determines the subtraction constant in the dispersion relation connecting the real and imaginary parts of the TCS and DVCS amplitudes [23, 28–30]. In the language of Regge theory [31–34], the D -term can be interpreted as originating from the t -channel exchange with $J = 0$ (the so-called fixed pole).

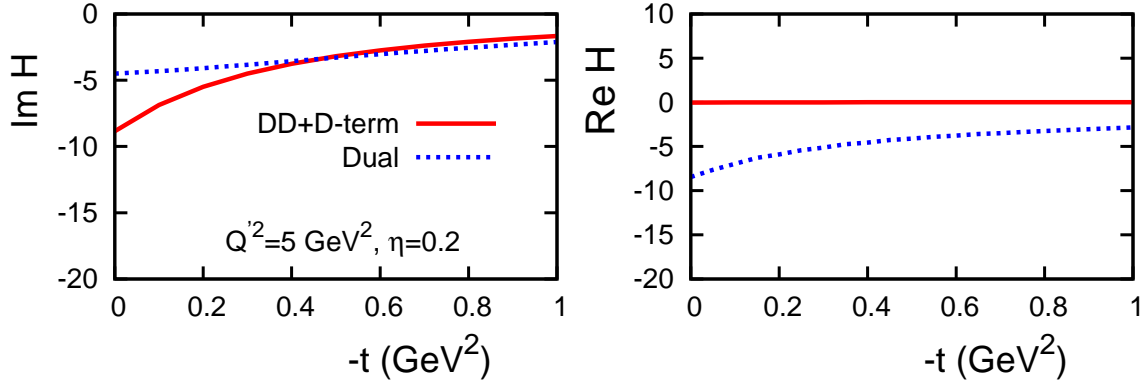


FIG. 7: Imaginary (left) and real (right) parts of the GPD H plotted as a function of $-t$ for $Q'^2 = 5 \text{ GeV}^2$ and $\eta = 0.2$ (*i.e.*, $\tau = 0.33$), where η is the TCS equivalent of ξ in DVCS. The curves show the same models as in Fig. 6.

C. TCS cross section and interference between TCS and BH amplitudes

In the leading-twist approximation, the TCS cross section has the following form [9]:

$$\frac{d\sigma_{\text{TCS}}}{dQ'^2 dt d\cos\theta d\varphi} \approx \frac{\alpha_{\text{em}}^3}{8\pi s^2} \frac{1}{Q'^2} \frac{1 + \cos^2\theta}{4} \sum_{\lambda, \lambda'} |M^{\lambda', \lambda-}|^2, \quad (7)$$

where α_{em} is the fine structure constant and $M^{\lambda', \lambda-}$ are helicity amplitudes, with λ (λ') denoting the helicity of the incoming (outgoing) photon. The TCS amplitude squared entering Eq. (7) is expressed in terms of the Compton form factors:

$$\begin{aligned} \frac{1}{2} \sum_{\lambda, \lambda'} |M^{\lambda', \lambda-}|^2 &= (1 - \eta^2)(|\mathcal{H}_1|^2 + |\tilde{\mathcal{H}}_1|^2) - 2\eta^2 \text{Re}(\mathcal{H}_1^* \mathcal{E}_1 + \tilde{\mathcal{H}}_1^* \tilde{\mathcal{E}}_1) \\ &\quad - \left(\eta^2 + \frac{t}{4m_N^2}\right) |\mathcal{E}_1|^2 - \eta^2 \frac{t}{4m_N^2} |\tilde{\mathcal{E}}_1|^2. \end{aligned} \quad (8)$$

Theoretical analyses [9, 35] have shown that the TCS cross section is smaller than the BH cross section for JLab 12 GeV kinematics. Figure ?? shows the unpolarized cross sections of BH and of TCS as a function of Q'^2 at $\eta=0.2$, $-t = 0.4 \text{ GeV}^2$, $\phi = 0^\circ, 360^\circ$ and for θ integrated over $[\pi/4, 3\pi/4]$. It is seen that TCS is suppressed by about 2 orders of magnitude with respect to BH.

However like in DVCS, the BH and TCS amplitudes also interfere. When the initial-state

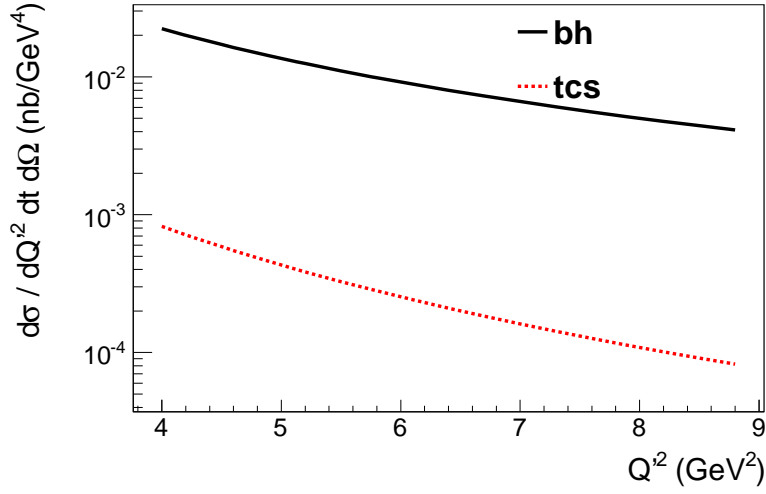


FIG. 8: Unpolarized cross section $\frac{d\sigma}{dQ'^2 dt d\phi d(\cos\theta)}$ for the process $\gamma P \rightarrow P' e^+ e^-$, for BH and TCS alone, as a function of Q'^2 , at $\eta=0.2$, $-t = 0.4 \text{ GeV}^2$, for $\theta = 45^\circ, 90^\circ$ for $\phi = 0^\circ, 360^\circ$ and for θ integrated over $[\pi/4, 3\pi/4]$.

photon is unpolarized, the interference term can be expressed as:

$$\begin{aligned} \frac{d\sigma_{\text{INT}}}{dQ'^2 dt d(\cos\theta) d\phi} &= -\frac{\alpha_{\text{em}}^3}{4\pi s^2} \frac{1}{-t} \frac{M}{Q'} \frac{1}{\tau\sqrt{1-\tau}} \frac{L_0}{L} \\ &\times \left[\cos\varphi \frac{1+\cos^2\theta}{\sin\theta} \Re e \tilde{M}^{--} - \cos 2\varphi \sqrt{2} \cos\theta \Re e \tilde{M}^{0-} \right. \\ &\left. + \cos 3\varphi \sin\theta \Re e \tilde{M}^{+-} + \mathcal{O}\left(\frac{1}{Q'}\right) \right], \end{aligned} \quad (9)$$

where M is the proton mass. The variable τ ,

$$\tau = \frac{Q'^2}{2(p \cdot q)} = \frac{Q'^2}{s - M^2}, \quad (10)$$

in TCS is the analog of the Bjorken variable $x_B = Q^2/(2p \cdot q)$ in DVCS. To leading twist accuracy,

$$\eta = \frac{\tau}{2 - \tau}, \quad (11)$$

where η is given by Eq. (5). In Eq. (9), L_0 and L originate from the product of final-state lepton propagators [9] and $\tilde{M}^{\mu'\mu}$ are interference helicity amplitudes, where μ (μ') denotes the helicity of the incoming (outgoing) photon. In the handbag approximation, the photon (parton) helicity is conserved and, as a result, the only surviving contribution in Eq. (9) comes from \tilde{M}^{--} :

$$\tilde{M}^{--} = \frac{2\sqrt{t_0 - t}}{M} \frac{1 - \eta}{1 + \eta} \left[F_1 \mathcal{H}_1 - \eta(F_1 + F_2) \tilde{\mathcal{H}}_1 - \frac{t}{4M^2} F_2 \mathcal{E}_1 \right], \quad (12)$$

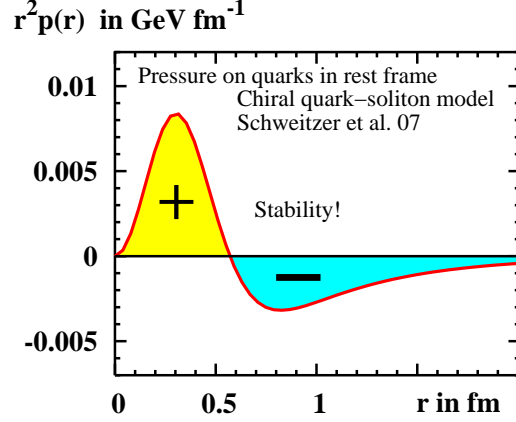


FIG. 9: Pressure experienced by quarks inside the nucleon calculated in the framework of the chiral quark-soliton model [26].

where $-t_0 = 4\eta^2 M^2 / (1 - \eta^2)$ is the minimal momentum transfer at a given η (modulo $1/Q'^2$ corrections), and F_1 and F_2 are the Dirac and Pauli elastic form factors of the proton, respectively.

Unpolarized photons (from a helicity-averaged electron beam) give access to the real part of the CFFs. With a longitudinally polarized electron beam, producing circularly polarized photons with polarization $\nu \neq 0$, one can simultaneously study both the real and imaginary parts of the helicity amplitudes using the full expression for the interference term [9]:

$$\begin{aligned}
\frac{d\sigma_{\text{INT}}}{dQ'^2 dt d(\cos\theta) d\varphi} = & -\frac{\alpha_{em}^3}{4\pi s^2} \frac{1}{-t} \frac{M}{Q'} \frac{1}{\tau\sqrt{1-\tau}} \frac{L_0}{L} \\
& \times \left(\left[\cos\varphi \frac{1+\cos^2\theta}{\sin\theta} \Re e \tilde{M}^{--} - \cos 2\varphi \sqrt{2} \cos\theta \Re e \tilde{M}^{0-} \right. \right. \\
& + \cos 3\varphi \sin\theta \Re e \tilde{M}^{+-} + \mathcal{O}\left(\frac{1}{Q'}\right) \left. \right] \\
& + \nu \left[\sin\varphi \frac{1+\cos^2\theta}{\sin\theta} \text{Im} \tilde{M}^{--} - \sin 2\varphi \sqrt{2} \cos\theta \Im m \tilde{M}^{0-} \right. \\
& \left. \left. + \sin 3\varphi \sin\theta \text{Im} \tilde{M}^{+-} + \mathcal{O}\left(\frac{1}{Q'}\right) \right] \right), \tag{13}
\end{aligned}$$

Under charge conjugation of the final-state lepton pair, which corresponds to the transformation $\varphi \rightarrow \varphi + \pi$, the TCS and BH cross sections are even, while the interference term is odd. This makes it possible to project out the TCS-BH interference through the weighted and θ -integrated cross section [9]:

$$\frac{dS}{dQ'^2 dt d\varphi} = \int_{\pi/4}^{3\pi/4} d\theta \frac{L(\theta, \varphi)}{L_0(\theta)} \frac{d\sigma}{dQ'^2 dt d\theta d\varphi}. \tag{14}$$

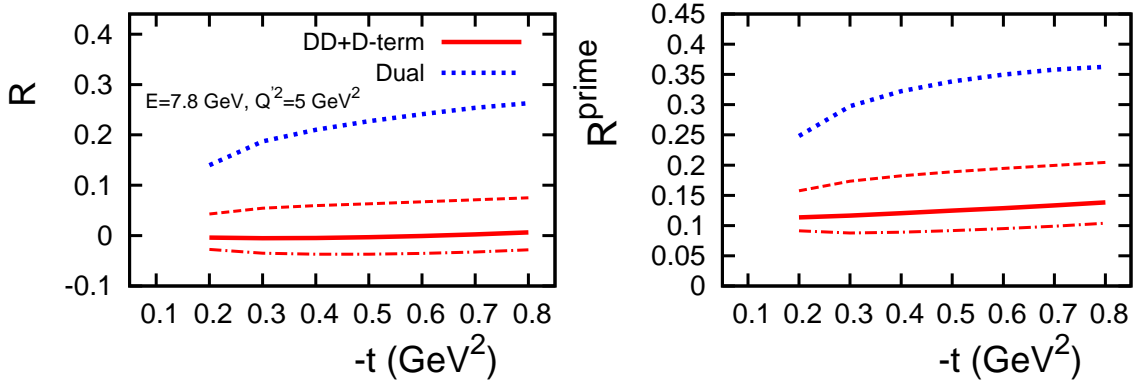


FIG. 10: Predictions for the cosine moment of the weighted cross section shown as a function of $-t$ at a fixed initial-state photon energy $E_\gamma = 7.8$ GeV and $Q^2 = 5$ GeV². The curves correspond to GPD models based on the dual parametrization [16–19] (blue) and the double distribution [20] (red), respectively. The three lower (red) curves correspond to different strengths of the D -term quantified by the parameter κ in Eq. (16). The moment R , defined in Eq. (15), is shown in the left panel, while the right panel shows the corresponding curves for R' . The latter is integrated over the θ - φ acceptance of the detector. The details are explained in Sect. 4. It is interesting to note that while the different integration contour changes the absolute value of R' compared with R , it does not diminish the sensitivity.

The contribution of, for instance, $\Re e \tilde{M}^{--}$, can now be obtained by taking the $\cos \varphi$ -moment of S [9]:

$$R = \frac{2 \int_0^{2\pi} d\varphi \cos \varphi \frac{dS}{dQ'^2 dt d\varphi}}{\int_0^{2\pi} d\varphi \frac{dS}{dQ'^2 dt d\varphi}}. \quad (15)$$

An example of the calculation of R as a function of $-t$ at a fixed initial-state photon energy $E_\gamma = 7.8$ GeV and $Q^2 = 5$ GeV² is shown in the left panel of Fig. 10. The curves show predictions of calculations based on two GPD models: the dual parametrization [16–19] (upper curve) and the double distribution [20] (lower three curves). The difference in the magnitude of R is quite significant, as would be expected given the difference in $\Re e H$ shown in Fig. 7. The three lower curves correspond to different strengths of the D -term [3] in the double distribution, as quantified by the parameter κ in Eq. (16). It is interesting to note that for the standard value of κ , the double distribution predicts a cancellation with the D -term resulting in a small $\Re e H$ – a feature absent in the dual parametrization. The right panel in Fig. 10 shows the same calculations performed within the θ - φ acceptance of the detector. The details are explained in

Sect. 4. In the calculations with the double distribution, for the GPD H we used:

$$H^q(x, \eta, t) = \int_{-1}^1 d\beta \int_{-1+|\beta|}^{1-|\beta|} d\alpha \delta(x - \beta - \alpha\eta) \pi(|\beta|, \alpha) q(\beta, t) + \kappa \frac{1}{N_f} \Theta(\eta - |x|) D(x/\eta, t), \quad (16)$$

where $\pi(\beta, \alpha)$ is the profile function that determines the degree of skewness, $q(\beta, t)$ is the off-diagonal quark parton distribution that reduces to the usual parton distribution in the $t = 0$ limit, $D(x/\eta, t)$ is the D -term, and $N_f = 3$ is the number of active quark flavors. Note that we introduced the coefficient κ in front of the D -term to vary the strength of its contribution. For the D -term, we used the standard expansion in terms of the Gegenbauer polynomials $C_n^{3/2}$:

$$D(z, t = 0) = -(1 - z^2)(d_1 C_1^{3/2}(z) + d_3 C_3^{3/2}(z) + d_5 C_5^{3/2}(z)). \quad (17)$$

The magnitude of the coefficients d_i in Eq. (17) was estimated in the chiral quark-soliton model at a low normalization scale [36]; QCD evolution to the needed values of Q'^2 somewhat decreases the values of the coefficients [4]. To test the sensitivity of R the D -term, we varied the parameter κ . The three curves in Fig. 10 correspond to $\kappa = 0.5$ (lower curve), $\kappa = 1$ (standard magnitude of the D -term), and $\kappa = 2$ (upper curve), respectively.

D. Cross sections and beam asymmetries

1. Decay angular dependencies of the unpolarized cross section

Fig. 11 shows the calculation by Ref. [37] of the ϕ -dependence of the 4-fold differential cross section $\frac{d\sigma_{BH}}{dQ'^2 dt d\phi d(\cos\theta)}$ for the $\gamma P \rightarrow P' e^+ e^-$ reaction (i.e. BH+TCS), at $\eta = 0.2$, $-t = 0.4$ GeV², $Q'^2 = 7$ GeV² and for 3 θ values. The ϕ -distribution depends on θ . As θ tends to 0° , the ϕ distribution peaks towards $\phi=180^\circ$ and as θ tends to 180° , the ϕ -distribution peaks towards $\phi=0^\circ$ (or 360°). There is a smooth transition between these two behaviors for intermediate θ values. For instance, at $\theta=90^\circ$, there are only two small "bumps" at $\phi=0^\circ$ and $\phi=180^\circ$.

These particular shapes are due to the BH process and its singularities. Indeed, in the BH process, when the electron (positron) is emitted in the direction of the initial photon, i.e. $\theta = 0^\circ$ ($\theta = 180^\circ$), the propagator of the positron (electron) becomes singular and creates a peak in the ϕ distribution at $\phi = 180^\circ$ ($\phi = 0^\circ$). Intuitively, $\theta = 0^\circ$ ($\theta = 180^\circ$) forces all particles to be in the same plane, i.e. $\phi = 180^\circ$ ($\phi = 0^\circ$). The kinematics $\theta = 0^\circ$, i.e. the electron is in the direction of the photon beam, corresponds to $\phi = 180^\circ$ because the virtual photon is emitted by the positron, not the electron.

We display also in Fig. 11 (left panel) the contribution of TCS alone. In this calculation, we have used only the GPD H . The inclusion of the other GPDs barely changes the result. In contrast to the BH, the TCS is almost flat in ϕ for all θ values. It is clear that the process

$\gamma P \rightarrow P' e^+ e^-$ is largely dominated by the BH. There is never less than one order of magnitude between BH and TCS.

In Fig. 11 (right panel), we show the curves BH+TCS as well as the BH alone for $\theta=45^\circ$ and $\theta=90^\circ$. Only at $\theta=90^\circ$, where one is far from the two BH singularities, we have a visible difference between the two curves and therefore a sensitivity to TCS. It is of the order of 30% at $\phi=180^\circ$. As one gets closer to one of the two BH singularities ($\theta=45^\circ$ for instance), the two curves BH and BH+TCS are essentially indistinguishable and there is no sensitivity to TCS.

Finally, we show in Fig. 11 the results of the calculations of Ref. [37] for BH+TCS and BH alone for θ integrated over the range $[\pi/4, 3\pi/4]$. In order to maximize count rates, it is interesting to integrate over θ . One still has a sensitivity to TCS. However, it is of the order of 5%, i.e. less than at fixed $\theta=90^\circ$: the integration over θ dilutes the sensitivity to TCS.

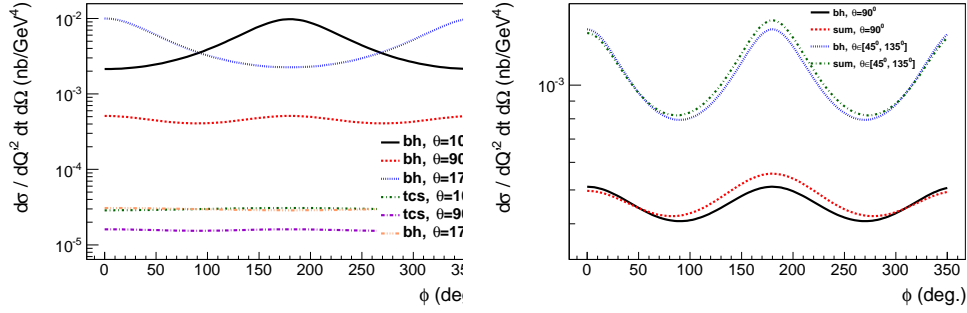


FIG. 11: Left panel: Unpolarized cross section $\frac{d\sigma}{dQ^2 dt d\phi d(\cos\theta)}$ for the process $\gamma P \rightarrow P' e^+ e^-$ (for BH + TCS and TCS alone) as a function of ϕ , at $\eta=0.2$, $-t = 0.4$ GeV², $Q'^2 = 7$ GeV² for different fixed θ values: 10° , 90° , 170° for the BH and for the TCS cross sections. Right panel: Comparison between unpolarized cross section for BH alone and for BH+TCS for $\theta = 45^\circ$, 90° and for θ integrated over $[\pi/4, 3\pi/4]$.

To emphasize the D-term sensitivity in unpolarized cross section, we also display in Fig. 12 the three-fold differential cross section $\frac{d\sigma_{BH}}{dQ^2 dt d\phi}$ for $\eta = 0.2$, $-t = 0.4$ GeV² and θ integrated over the range $[\pi/4, 3\pi/4]$, calculated by Ref. [38]. It modifies the amplitude of the cross section, mostly at $\phi = 0$ and at $\phi = \pi$, by about 10%.

2. Circularly polarized beam spin asymmetry

The beam asymmetry with a circularly polarized beam is defined as:

$$A_{\odot U} = \frac{\sigma^+ - \sigma^-}{\sigma^+ + \sigma^-}, \quad (18)$$

where σ^\pm stands for the 4-fold differential cross sections $\frac{d\sigma}{dQ^2 dt d\phi d(\cos\theta)}$ for the two photon spin states, right and left polarized. We display in Fig. 13 (top panel) the results for $A_{\odot U}$ as a

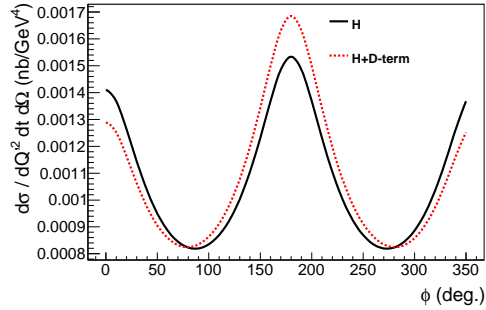


FIG. 12: Unpolarized cross section $\frac{d\sigma}{dQ^2 dt d\phi d(\cos\theta)}$ for the process $\gamma P \rightarrow P' e^+ e^-$ (for BH + TCS and TCS alone) as a function of ϕ , at $\eta=0.2$, $-t = 0.4 \text{ GeV}^2$, $Q'^2 = 7 \text{ GeV}^2$ and for θ integrated over $[\pi/4, 3\pi/4]$, with of without the D-term included in calculations.

function of ϕ at $Q'^2 = 7 \text{ GeV}^2$, $\eta = 0.2$, $-t = 0.4 \text{ GeV}^2$ for θ integrated over $[45^\circ, 135^\circ]$, as calculated by Ref. [38]. We observe that the BH doesn't produce any asymmetry. Any non-zero therefore reflects the contribution from TCS. This is due to the fact that this observable is sensitive to the imaginary part of the amplitude and that the BH amplitude is purely real. The different curves correspond to different GPDs parametrizations for TCS. In Fig. 14, we show for $\eta = 0.2$, $Q'^2 = 7 \text{ GeV}^2$, $\phi = 90^\circ$ and θ integrated over $[45^\circ, 135^\circ]$, the t -dependence of $A_{\odot U}$ and its sensitivity to different GPDs. We notice that the magnitude of $A_{\odot U}$ increases with $|t|$ and that there is a sensitivity of this observable to all four GPDs. We also display in this figure the results with the factorized ansatz for the t -dependence of the H GPD in order to illustrate the model-dependence of the calculation.

E. NLO corrections

Timelike Compton Scattering (TCS) shares many features with spacelike DVCS and allows to access the same GPDs. The amplitudes of these two reactions are related at Born order by a simple complex conjugation, but they significantly differ at next to leading order (NLO) in the strong coupling constant α_s [39]. In the recent paper [40] it was shown that the Born amplitudes of DVCS and TCS processes get sizeable $O(\alpha_s)$ corrections and, even at moderate energies, the gluonic contributions are by no means negligible. We stress that the timelike and spacelike cases are complementary and that their difference deserves much special attention.

Including gluon coefficient function appearing first at NLO, and NLO corrections to the quark coefficient functions [14, 41–44] entering the TCS amplitudes, modifies significantly the values of the timelike Compton form factors. Results are shown for two GPD models based on Double Distributions (DDs): the so-called Goloskokov-Kroll (or GK) model [45–48], and a model based on the simple factorizing ansatz for the t -dependence [9] with MSTW08 PDFs [49].

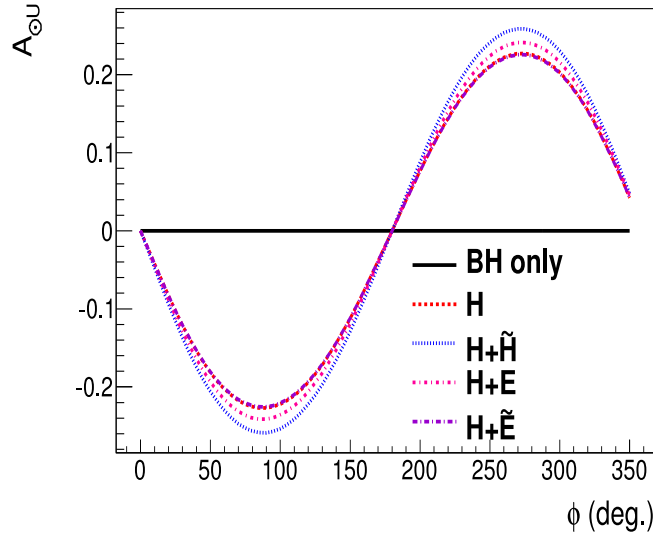


FIG. 13: The $A_{\odot U}$ for $\theta \in [45^\circ, 135^\circ]$ using different GPDs parametrizations for TCS. The calculations are done for $Q'^2 = 7 \text{ GeV}^2$, $\eta = 0.2$, $-t = 0.4 \text{ GeV}^2$.

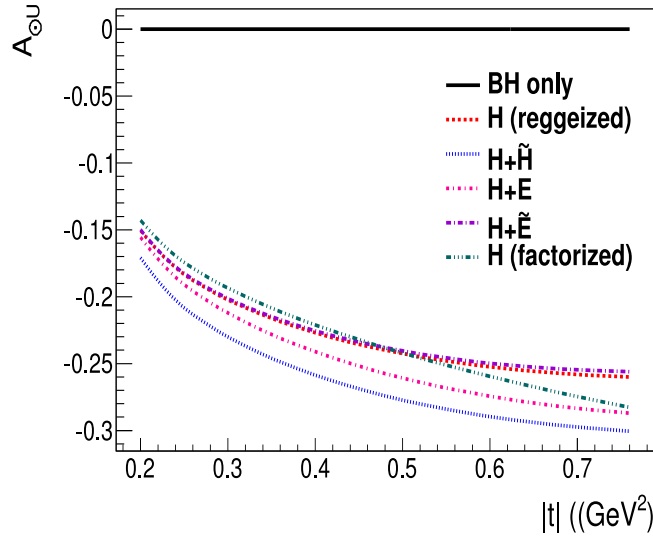


FIG. 14: The $A_{\odot U}$ asymmetry as a function of t for BH+TCS at $\eta = 0.2$, $Q'^2 = 7 \text{ GeV}^2$, $\phi = 90^\circ$ and θ integrated over $[45^\circ, 135^\circ]$. TCS is calculated with different GPDs.

The consequence of a Polyakov-Weiss D -term [21], following [9] and [4] is explored with the use of the parametrization obtained by a fit to the chiral soliton model [50].

1. The TCS amplitudes

After proper renormalization, the full Compton scattering amplitude (for both DVCS or TCS) reads in its factorized form (at factorization scale μ_F)

$$\begin{aligned} \mathcal{A}^{\mu\nu} = & -g_T^{\mu\nu} \int_{-1}^1 dx \left[\sum_q^{n_F} T^q(x) F^q(x) + T^g(x) F^g(x) \right] \\ & + i\epsilon_T^{\mu\nu} \int_{-1}^1 dx \left[\sum_q^{n_F} \tilde{T}^q(x) \tilde{F}^q(x) + \tilde{T}^g(x) \tilde{F}^g(x) \right], \end{aligned} \quad (19)$$

where we omitted the explicit skewness dependence. The renormalized coefficient functions are given by

$$\begin{aligned} T^q(x) &= \left[C_0^q(x) + C_1^q(x) + \ln\left(\frac{Q^2}{\mu_F^2}\right) \cdot C_{coll}^q(x) \right] - (x \rightarrow -x), \\ T^g(x) &= \left[C_1^g(x) + \ln\left(\frac{Q^2}{\mu_F^2}\right) \cdot C_{coll}^g(x) \right] + (x \rightarrow -x), \\ \tilde{T}^q(x) &= \left[\tilde{C}_0^q(x) + \tilde{C}_1^q(x) + \ln\left(\frac{Q^2}{\mu_F^2}\right) \cdot \tilde{C}_{coll}^q(x) \right] + (x \rightarrow -x), \\ \tilde{T}^g(x) &= \left[\tilde{C}_1^g(x) + \ln\left(\frac{Q^2}{\mu_F^2}\right) \cdot \tilde{C}_{coll}^g(x) \right] - (x \rightarrow -x). \end{aligned} \quad (20)$$

The difference between the DVCS and the TCS cases is the consequence of analyticity (in Q^2) which leads to the relation [39]:

$${}^{TCS}T(x, \eta) = \pm ({}^{DVCS}T(x, \xi = \eta) + i\pi C_{coll}(x, \xi = \eta))^*, \quad (21)$$

where $+$ ($-$) sign corresponds to the vector (axial) case.

2. Timelike Compton Form Factors

The timelike Compton Form Factors (CFF) at NLO, \mathcal{H} and $\tilde{\mathcal{H}}$, defined as

$$\begin{aligned} \mathcal{H}(\eta, t) &= + \int_{-1}^1 dx \left(\sum_q T^q(x, \eta) H^q(x, \eta, t) + T^g(x, \eta) H^g(x, \eta, t) \right) \\ \tilde{\mathcal{H}}(\eta, t) &= - \int_{-1}^1 dx \left(\sum_q \tilde{T}^q(x, \eta) \tilde{H}^q(x, \eta, t) + \tilde{T}^g(x, \eta) \tilde{H}^g(x, \eta, t) \right), \end{aligned} \quad (22)$$

are the GPD dependent quantities which enter the amplitudes. For TCS they are defined through relations such as [9]

$$\mathcal{A}^{\mu\nu}(\eta, t) = -e^2 \frac{1}{(P_+ P'_+)} \bar{u}(P') \left[g_T^{\mu\nu} \left(\mathcal{H}(\eta, t) \gamma^+ + \mathcal{E}(\eta, t) \frac{i\sigma^{+\rho} \Delta_\rho}{2M} \right) + i\epsilon_T^{\mu\nu} \left(\tilde{\mathcal{H}}(\eta, t) \gamma^+ \gamma_5 + \tilde{\mathcal{E}}(\eta, t) \frac{\Delta^+ \gamma_5}{2M} \right) \right] u(P). \quad (23)$$

We present our results for $Q^2 = \mu_F^2 = \mu_R^2 = 4 \text{ GeV}^2$, and use the value $\alpha_S = 0.3$.

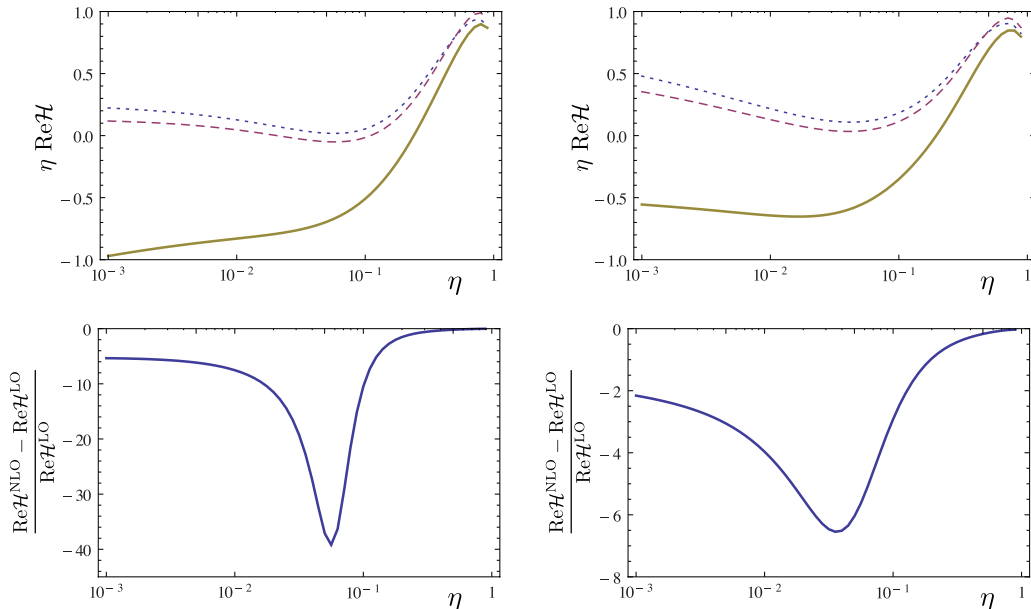


FIG. 15: The real part of the *timelike* Compton Form Factor \mathcal{H} multiplied by η , as a function of η in the double distribution model based on Goloskokov-Kroll (upper left) and MSTW08 (upper right) parametrizations, for $\mu_F^2 = Q^2 = 4 \text{ GeV}^2$ and $t = -0.1 \text{ GeV}^2$. Below the ratios of the NLO correction to LO result of the corresponding models.

To show the importance of including NLO effects in the timelike CFFs relevant to timelike Compton scattering, we plot in Fig. 15 and Fig. 16, the real and imaginary parts of the CFF \mathcal{H} for the GK and the MSTW08 models of GPDs, for the invariant mass of the lepton pair $Q'^2 = 4 \text{ GeV}^2$, $t = -0.1 \text{ GeV}^2$. For the imaginary part the correction does not exceed 40%. In the real part, the correction is of the order of few hundred percent. We observe that the main part of that large correction comes from the contribution of gluonic GPDs.

The D -term contribution to the CFF is a η -independent quantity and it has both a real and an imaginary parts at NLO. We show in Tab. I the values of this D -term contribution in the LO and NLO cases. Its relative effect on the imaginary part of the CFF decreases significantly when η decreases, from 10 to 1 and 0.1% when η decreases from 0.1 to 0.01 and to 0.001.

We then compare TCS and DVCS by plotting the ratio of NLO corrections on Fig. 17. There is a striking difference in the magnitude of the corrections to the real part of CFFs, mostly insensitive to the choice of GPD parametrizations. As discussed in Ref. [39], this is a consequence of Eq. (21) which by adding a phase to the dominant imaginary part of the spacelike CFF at small skewness, gives rise to a sizeable real part of the corresponding CFF in the timelike case.

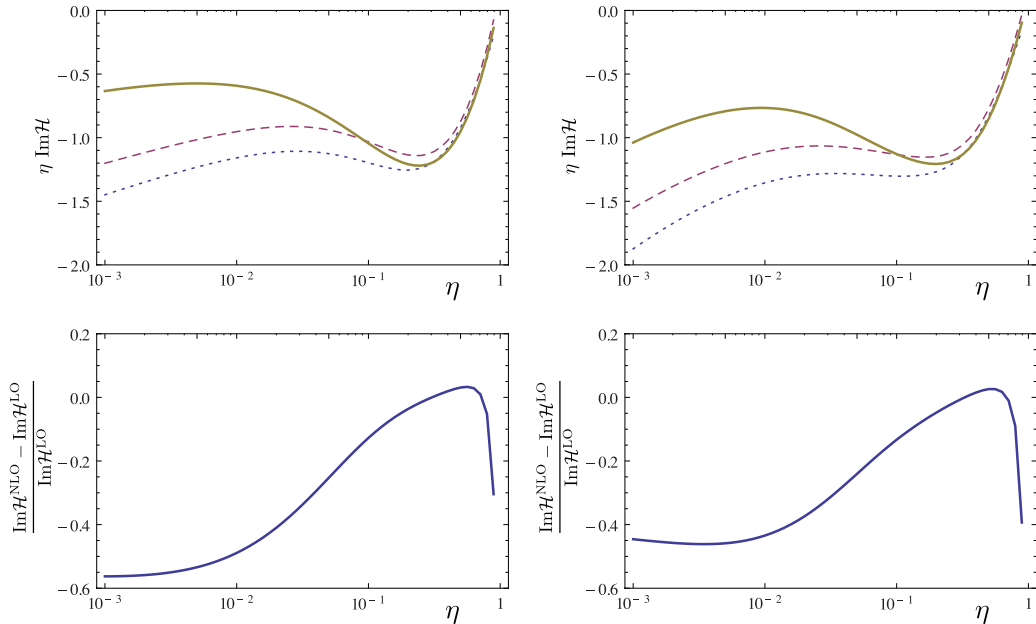


FIG. 16: The imaginary part of the *timelike* Compton Form Factor \mathcal{H} multiplied by η , as a function of η in the double distribution model based on Goloskokov-Kroll (upper left) and MSTW08 (upper right) parametrizations, for $\mu_F^2 = Q^2 = 4 \text{ GeV}^2$ and $t = -0.1 \text{ GeV}^2$. Below the ratios of the NLO correction to LO result of the corresponding models.

	$\text{Re}\mathcal{H}_{\mathcal{D}}$	$\text{Im}\mathcal{H}_{\mathcal{D}}$
LO	-2.59	0
NLO quark contribution	-0.16	-0.85
NLO gluon contribution	0.18	0.16
Full NLO	-2.57	-0.69

TABLE I: Different contributions to the D -term. The values of the real part coincides for spacelike and timelike CFF \mathcal{H} , while the imaginary part is non-vanishing only for the timelike case.

Such large corrections to the real part of CFFs will have a significant influence on observables which depend on the interference of the TCS process with the Bethe-Heitler amplitude, *i.e.* connected to the azimuthal angular distribution of the leptons.

In the context of the large NLO order corrections it is important to investigate the stability of the full NLO result with respect to the choice of the factorization scale μ_F . In Fig. 18 we illustrate this issue with a real and imaginary part of the CFF H multiplied by skewness η plotted for $\frac{Q^2}{\mu_F^2} = \{1, 2, 3, 4\}$. Indeed we see that for small values of eta, factorization scale dependence is very strong, but for the values corresponding to JLab kinematics ($\eta > 0.1$) the

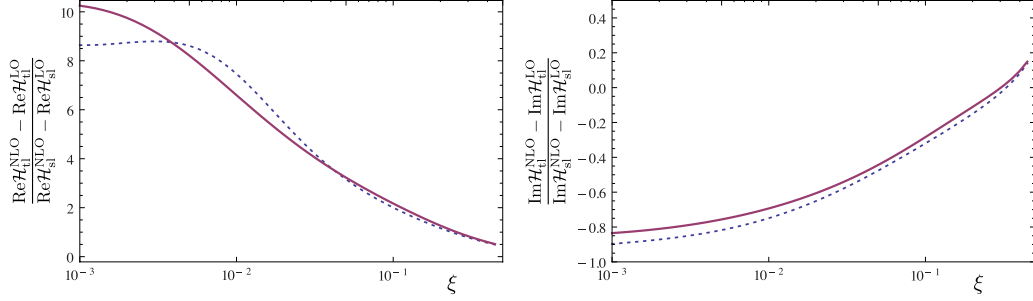


FIG. 17: The ratio of the timelike to spacelike NLO corrections in the real (left) and imaginary (right) part of the Compton Form Factor \mathcal{H} , as a function of ξ in the double distribution model based on the Goloskokov-Kroll (dashed) and MSTW08 (solid) parametrizations, for $\mu_F^2 = Q^2 = 4 \text{ GeV}^2$ and $t = -0.1 \text{ GeV}^2$. For comparison timelike CFFs were calculated at $\eta = \xi$.

result is very stable.

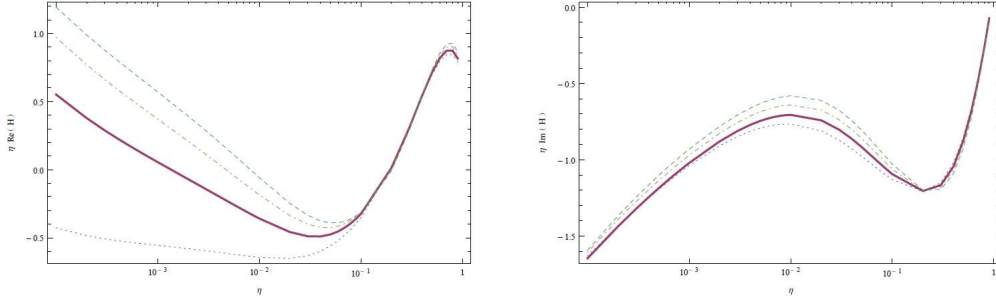


FIG. 18: Full NLO result for real(left) and imaginary(right) part of the CFF \mathcal{H} multiplied by skewness η for the $Q^2 = 4 \text{ GeV}^2$, $t = -0.1 \text{ GeV}^2$ and various choices of the factorization scale $\frac{Q^2}{\mu_F^2} = \{1, 2, 3, 4\}$. We see that for JLab kinematics result is very stable.

3. Cross sections and asymmetries

Let us now pass to our estimates for the observables in TCS. Generally we observe that the inclusion of the NLO corrections is more important at small skewness. We also see that the Bethe-Heitler dominates the integrated cross-section for this kinematics. In consequence, more differential observables, as the azimuthal ϕ dependence (with angles θ and ϕ defined in Ref. [9]) reveal in a better way the different contributions. Moreover simple ϕ dependence of the interference term allows for an easy access to the real part of the CFFs which, as we observed in

Fig. 15, is subject to big NLO corrections. We indeed observe that effect on the Fig. 19, which shows the ϕ dependence of the unpolarized differential cross sections for pure BH process, and with a LO and NLO corrections to the interference term.

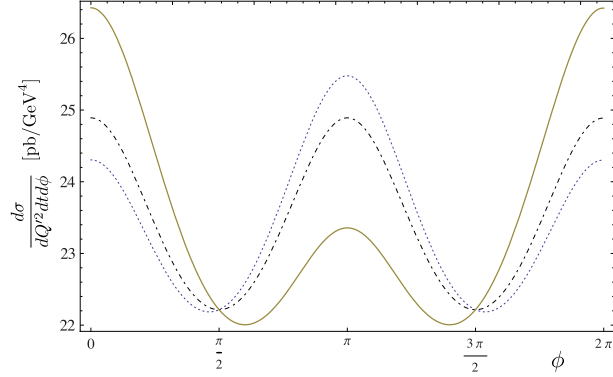


FIG. 19: The ϕ dependence of the cross-section at $E_\gamma = 10$ GeV, $Q^2 = \mu_F^2 = 4$ GeV², and $t = -0.1$ GeV² integrated over $\theta \in (\pi/4, 3\pi/4)$: pure Bethe-Heitler contribution (dash-dotted), Bethe-Heitler plus interference contribution at LO (dotted) and NLO (solid).

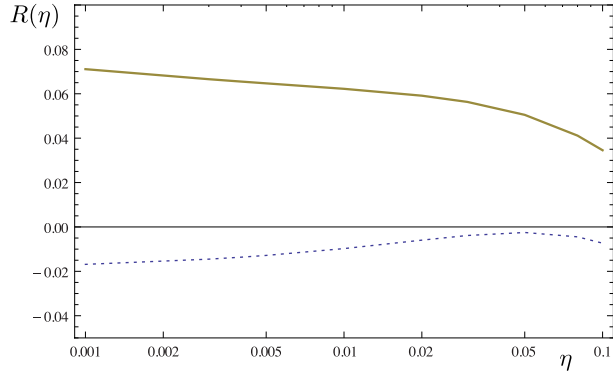


FIG. 20: Ratio R defined by Eq. (24) as a function of η , for $Q^2 = \mu_F^2 = 4$ GeV² and $t = -0.1$ GeV². The dotted line represents LO contribution and the solid line represents NLO result.

To quantify how big the deviation is from the pure Bethe-Heitler process in the unpolarized cross section we calculate (see Fig. 20) the ratio R, defined in Ref. [9] by

$$R(\eta) = \frac{2 \int_0^{2\pi} d\varphi \cos \varphi \frac{dS}{dQ^2 dt d\varphi}}{\int_0^{2\pi} d\varphi \frac{dS}{dQ^2 dt d\varphi}}, \quad (24)$$

where S is a weighted cross section given by Eq. (43) of Ref. [9]. It is plotted in Fig. 20 as a function of the skewness η for $Q^2 = \mu^2 = 4$ GeV², and $t = -0.2$ GeV². In the leading twist the

numerator is linear in the real part of the CFFs, and the denominator, for the kinematics we consider, is dominated by the Bethe - Heitler contribution. The inclusion of NLO corrections to the TCS amplitude is indeed dramatic for such an observable and includes also change of sign.

Imaginary parts of the CFFs are accessible through observables making use of photon circular polarizations [9]. The photon beam circular polarization asymmetry

$$A = \frac{\sigma^+ - \sigma^-}{\sigma^+ + \sigma^-}, \quad (25)$$

is shown on the left part of Fig. 21, as a function of ϕ for the kinematic variables relevant for JLab: $Q^2 = 4 \text{ GeV}^2 = \mu_F^2$, $t = -0.1 \text{ GeV}^2$ and $E_\gamma = 10 \text{ GeV}$ (which corresponds to $\eta \approx 0.11$). The same quantity is shown on the right panel of Fig. 21 as a function of η for $\phi = \pi/2$ and $Q^2 = 4 \text{ GeV}^2 = \mu_F^2$. The effect of the NLO corrections on that observable is rather large, around 10% in the η range most relevant for JLab kinematics.

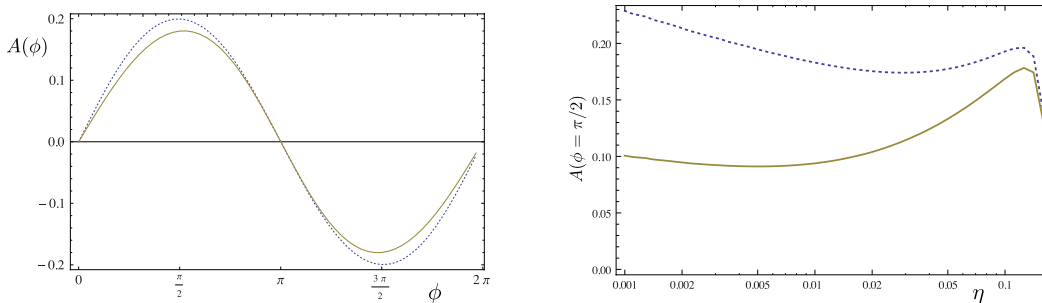


FIG. 21: (Left) Photon beam circular polarization asymmetry as a function of ϕ , for $t = -0.1 \text{ GeV}^2$, $Q^2 = \mu_F^2 = 4 \text{ GeV}^2$, integrated over $\theta \in (\pi/4, 3\pi/4)$ and for $E_\gamma = 10 \text{ GeV}$ ($\eta \approx 0.11$). (Right) The η dependence of the photon beam circular polarization asymmetry for $Q^2 = \mu_F^2 = 4 \text{ GeV}^2$, and $t = -0.2 \text{ GeV}^2$ integrated over $\theta \in (\pi/4, 3\pi/4)$. The LO result is shown as the dotted line, the full NLO result by the solid line.

F. Amplitude analysis of Compton form factors

At leading twist and leading order QCD, the GPDs and the CFFs involved in TCS and DVCS are related: the amplitudes are complex conjugates of one another. The interest of TCS is two-fold: 1/prove this universality of the GPDs, by showing that the same GPDs and CFFs can describe both the TCS and DVCS data (possibly with NLO corrections, in principle under control); 2/if so, use the new TCS observables to further constrain the fits of CFFs, currently extracted with only the DVCS data, by fitting simultaneously TCS and DVCS observables.

We recall that GPDs are not directly accessible in TCS and DVCS, but only CFFs. These latter depend only on t and ξ if Q^2 (Q'^2) evolution is neglected. In order to estimate

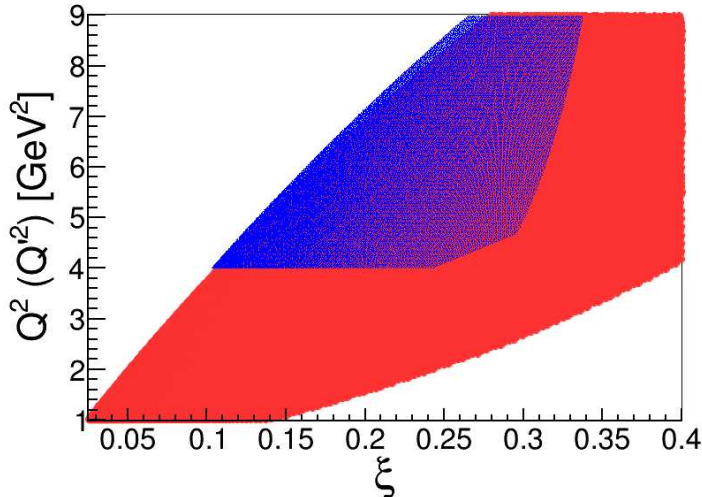


FIG. 22: Kinematical domain accessible as a function of ξ and Q^2 for DVCS (red plain surface) and in ξ or η and Q^2 for TCS (blue dotted surface) with an 11 GeV electron beam. For DVCS, the cuts $0 < -t < 1 \text{ GeV}^2$ and $s > 4 \text{ GeV}^2$ have been applied and for TCS, the cuts $5 < E_{\text{gamma}} < 11 \text{ GeV}$, $0 < -t < 1 \text{ GeV}^2$ and $4 < Q^2 < 9 \text{ GeV}^2$ have been applied.

the impact of TCS data on the extraction of CFFs, we have used the fitting algorithm of references [11, 38, 51–53]. The code was initially developed for the DVCS process and it consists in fitting simultaneously various experimental observables at a given kinematical point, i.e. η , t and Q^2 , with the 8 quark helicity-conserving CFFs: $Re\{\mathcal{H}\}$, $Re\{\mathcal{E}\}$, $Re\{\tilde{\mathcal{H}}\}$, $Re\{\tilde{\mathcal{E}}\}$, $Im\{\mathcal{H}\}$, $Im\{\mathcal{E}\}$, $Im\{\tilde{\mathcal{H}}\}$, $Im\{\tilde{\mathcal{E}}\}$, as free parameters. Given the well-known leading-twist and leading order TCS and BH amplitude, the algorithm seeks to find, by the least-square technique, the set of CFFs which minimizes the difference between the theory and the data, at a given t and ξ point. This approach has been very successful for the DVCS process, allowing to extract, at the $\approx 30\%$ level, from various beam- or target-polarized observables, three CFFs ($Re\{\mathcal{H}\}$, $Im\{\mathcal{H}\}$, and $Im\{\tilde{\mathcal{H}}\}$) at JLab and HERMES kinematics.

The algorithm has recently be extended to the TCS reaction. In particular, it now allows to fit simultaneously DVCS and TCS (pseudo-)data. We generated DVCS and TCS pseudo-data at the kinematics $E_e=11 \text{ GeV}$, $\eta=0.2$, $Q^2=3 \text{ GeV}^2$, $-t=0.4 \text{ GeV}^2$ and $Q'^2=7 \text{ GeV}^2$ for four observables: DVCS unpolarized and beam polarized cross sections, TCS unpolarized and beam polarized cross sections (for TCS, we will consider the photon beam linear and circular polarizations). Fig. 22 shows that this is a kinematics which is accessible in both TCS and DVCS for JLab 12 GeV kinematics.

We studied different uncertainties for the DVCS and TCS observables. Table II shows the impact of adding TCS observables to DVCS observables in the fit. With DVCS alone, by fitting

the unpolarized and beam polarized cross sections, each with 5% uncertainty, one is able to recover the originally generated $Im\{\mathcal{H}\}$ and $Re\{\mathcal{H}\}$ CFFs with, in average, $\approx 40\%$ and $\approx 100\%$ uncertainties. We recall that these two particular observables are dominated by the H GPD and that it is rather natural that these two CFFs come out of the fit. We also recall that in this procedure, the errors on the extracted CFFs is not directly proportional to the precision of the experimental data. They rather reflect the influence (or our ignorance) of the non-dominant CFFs (which are allowed to vary within well conservative limits).

Adding the TCS unpolarized and beam polarized cross sections, each measured with 15% uncertainty, decreases the error bars on $Im\{\mathcal{H}\}$ and $Re\{\mathcal{H}\}$. In particular, with a circularly polarized photon beam, one obtains now $\approx 20\%$ uncertainty for $Im\{\mathcal{H}\}$ and with a linearly polarized photon beam $\approx 50\%$ uncertainty for $Re\{\mathcal{H}\}$. One thus notes the factor ≈ 2 gain for both CFFs. We recall that the single spin asymmetries with a circularly polarized photon beam are sensitive to the imaginary part of the TCS amplitudes while those with a linearly polarized photon beam are sensitive to the real part [37]. Reducing the error bars on the TCS observables to 5% further decreases the error bars on the CFFs.

In summary, adding more observables to the CFF fits, with reasonably achievable error bars, allows a significant gain (factor 2 from our simulations) on the extraction of the CFFs $Im\{\mathcal{H}\}$ and $Re\{\mathcal{H}\}$.

	$(\sigma, \Delta\sigma_{LU})$ DVCS 5%	$(\sigma, \Delta\sigma_{LU})$ DVCS 5% + TCS $_{\ell}$ 15%	$(\sigma, \Delta\sigma_{LU})$ DVCS 5% + TCS $_c$ 15%	$(\sigma, \Delta\sigma_{LU})$ DVCS 5% + TCS $_{\ell}$ 5%	$(\sigma, \Delta\sigma_{LU})$ DVCS 5% + TCS $_c$ 5%
$\sigma^+(Re\{\mathcal{H}\})$	+121%	+92%	+80%	+54%	+55%
$\sigma^-(Re\{\mathcal{H}\})$	-84%	-79%	-83%	-44%	-45%
$\sigma^+(Im\{\mathcal{H}\})$	+23%	+20%	+15%	+11%	+12%
$\sigma^-(Im\{\mathcal{H}\})$	-50%	-40%	-21%	-27%	-19%

TABLE II: The table shows, for 5 different fits configurations (number of observables and uncertainties being varied) the uncertainties on the extracted $Im\{\mathcal{H}\}$ and $Re\{\mathcal{H}\}$ CFFs (which are the dominant contributors to the fitted observables). Since the fit is under-constrained (eight free parameters for only 2 observables to be fitted), the problem is not linear and the error bars are asymmetric. σ stand for the unpolarized cross section and $\Delta\sigma_{LU}$ for the beam polarized cross section (electron for DVCS and photon for TCS). The index ℓ stands for a linearly polarized beam and c for a circularly polarized photon beam. The percentages indicate the uncertainty on the data.

G. Comment on dispersion analysis

Dispersion relations provide a very powerful and model-independent method to relate the real and imaginary parts of scattering amplitudes based on such general properties as analyticity and crossing symmetry. For hard exclusive reactions, dispersion relations have been established and analyzed for DVCS, double DVCS (where the incoming photon has a spacelike virtuality and the outgoing photon is timelike), and for exclusive meson production [28–30].

For instance, for the CFF $\mathcal{H}^{q[+]}$ (the superscript $[+]$ indicates the singlet combination corresponding to $q + \bar{q}$), one obtains the dispersion relation [29]:

$$\Re\mathcal{H}^{q[+]}(\xi) = \frac{1}{\pi} \int_1^\infty d\omega \Im m C^{q[+]}(\omega) \int_{-1}^1 dx \left\{ H^q(x, \frac{x}{\omega}) \left[\frac{1}{\omega\xi - x} - \frac{1}{\omega\xi + x} \right] + \frac{2D^q(x)}{\omega - x} \right\}, \quad (26)$$

where $C^{q[+]}$ is the process-dependent hard-scattering kernel. The D -term enters the dispersion relation as a subtraction constant, *i.e.*, it gives an energy-independent contribution to $\Re\mathcal{H}^{q[+]}$. The importance of the dispersion relation in Eq. (26) is that it quantifies the amount of information on GPDs that can be extracted from the real and imaginary parts of CFFs or, more generally, from amplitudes of exclusive processes. In addition, it provides a practical consistency check for models of GPDs. While dispersion relations for the TCS amplitudes have not yet been worked out, there should be no major difficulty in establishing them analogously to the cases that have already been considered.

H. Results from CLAS 6 GeV data

Our proposed SoLID experiment builds upon experience gained from the analysis of CLAS 6 GeV data, which has established the technique for carrying out exclusive photoproduction experiments with quasi-real photons that we propose for this experiment with SoLID. As will be discussed in Sec. 3B, this requires the detection of all final-state particles except the scattered electron, for which the missing mass and missing transverse momentum are constrained to be very small. More specifically, this technique has also been successfully applied to pilot measurements of timelike Compton scattering using the CLAS e1-6 and e1f data sets. The results from this CLAS Approved Analysis (CAA-DP09-01) have been documented in Ref. [54]. It demonstrated an impressive pion pair rejection of factor of 2.07×10^{-7} . Measuring the ϕ cross section in parallel with TCS showed that the flux of quasi-real photons is well understood. The results from the above analysis could also be compared with an TCS analysis using the g12 data set, which was the only high-energy CLAS data set with tagged real photons (up to 5.7 GeV) that utilized the Cherenkov counters. These had been made ready specifically for TCS and other e^+e^- physics. The analysis of the g12 data is still ongoing, but preliminary results seems

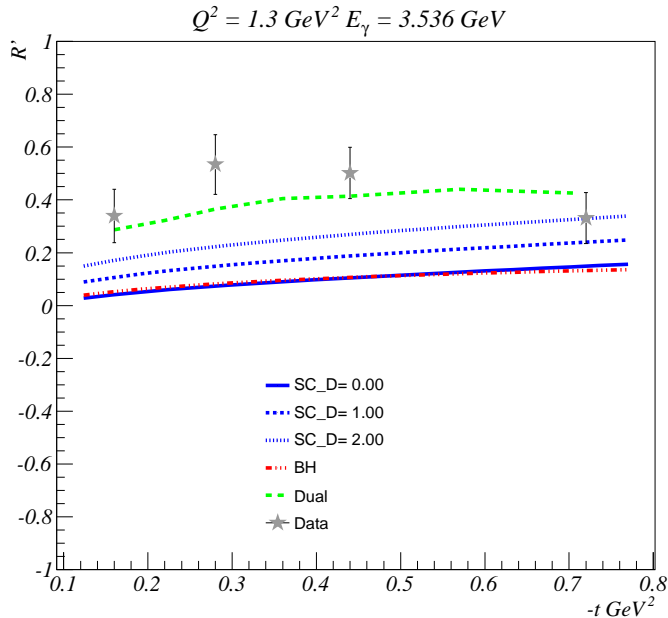


FIG. 23: The cosine moment of the weighted cross section, R' , in the CLAS acceptance compared to GPD model calculations based on the dual parametrization [16–19] (upper, green curve), and the double distribution [20] (lower, blue curves) for three weights applied to the D -term. The BH-contribution is shown in red.

to be in line with what was obtained with the quasi-real photon technique. The tagged-photon beam will also make it possible to do an independent determination of the photon flux, and offer an opportunity to explore event topologies with only two out of the three final-state particles detected.

In addition to demonstrating the feasibility of the proposed measurement, the pilot experiments at 6 GeV stimulated the development of new analysis methods. An example of this was the introduction of the cosine moment R' , evaluated within the acceptance of the detector in the $\varphi_{CM} - \theta_{CM}$ plane (the lepton c.m. angles φ and θ are defined in Fig. 3). Whereas the original definition of R implies using the integration ranges shown in Eqs.(14) and (15), R' adds an function $a(\theta_{CM}, \varphi_{CM})$ corresponding to the detector acceptance for a given kinematic bin. Utilizing the same acceptance function for both the experimental and theoretical evaluations allows a straightforward comparison between data and predictions based on various GPD models. The difference between R' and R is discussed in more detail in Sec. ?? together with the projected results.

Fig. 23 shows R' extracted from the combined e1-6 and e1f data sets for four bins in $-t$, compared with two GPD model calculations based on the dual parametrization [16–19] and

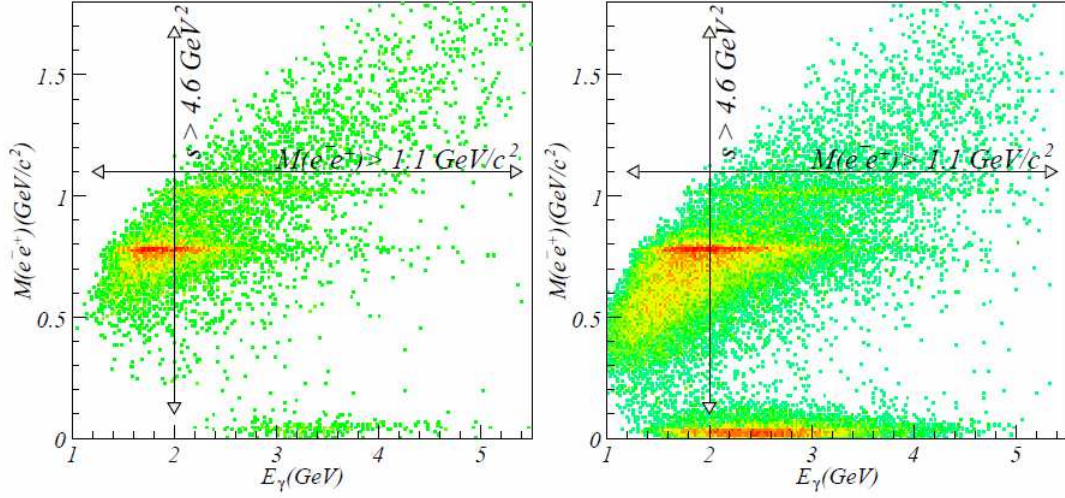


FIG. 24: e^+e^- invariant mass vs. quasi-real photon energy for the e1-6 (left) and e1f (right) data sets. Only events with M_{ee} above the ϕ mass were used for TCS analysis at 6 GeV.

double distribution [20], respectively. Results from the latter are shown with three weights for the contribution from the D -term (0, 1, and 2). Both the experimental and theoretical points shown here were evaluated at the average value for the bin, but an event-by-event approach will be adopted in the future.

However, despite the usefulness of the 6 GeV data for developing the TCS program, only the 12 GeV era will provide the required luminosity and kinematic coverage. In particular, the higher beam energy will make it possible to study a range of invariant lepton pair masses where there are no meson resonances that complicate the interpretation of the measurement. As shown in Fig. 24, only data above the ϕ mass were used for TCS analysis at 6 GeV, but at 12 GeV it will be possible to move this range above the mass of the ρ' .

3. EXPERIMENTAL SETUP

We propose to study photoproduction of lepton pairs, $\gamma p \rightarrow l^+ l^- p'$, in a wide range of kinematics using the SoLID detector in Hall A and a 11 GeV longitudinally polarized electron beam impinging on a hydrogen target. Because there's no real photon beam available in Hall A, the analysis will use the fully exclusive reaction

$$ep \rightarrow e^+ e^- p'(e') \quad (27)$$

where the electron (e') scatters at a small angle ($\sim 0^\circ$), and escapes detection in SoLID. This will include both real photoproduction due to the extended target and quasi-real photoproduction in data. In Eq. (27), $e^+ e^-$ is the produced lepton pair, and p' is the recoil proton. The exclusivity of the reaction is ensured by detecting all final-state particles. The missing scattered electron will be deduced from $e^+ e^- p'$ and cutting on the missing-particle kinematics, in a similar manner as in the TCS analysis of the CLAS 6 GeV data [54].

Because the multiple final state particle detection in wide kinematics, large acceptance detectors like CLAS12 and SoLID are ideal for the measurement. The SoLID J/ψ experiment E12-12-006 [2] contains all the needed equipments to detector the TCS final states $e^+ e^- p$. And because the J/ψ experiment also have decay $e^+ e^-$ pair and their kinematic distribution is similar to TCS, it is possible to have a common trigger, thus the data can be collected in parallel.

Since the TCS cross section will not be measured separately but in combination with the much larger Bethe-Heitler (BH) cross section with which it interferes, the rate estimates for TCS were based on the BH cross section as given in Ref. [55].

For either BH and TCS with varying photon energy, the five-fold differential cross section is

$$\frac{d^5\sigma}{dQ^2 dt d\eta d(\cos\theta_{CM}) d(\varphi_{CM})} \quad (28)$$

where t four-momentum transfer squared, Q^2 is invariant mass square of the decay lepton pair, and θ_{CM} and φ_{CM} are the lepton polar and azimuthal angles in the ($e^+ e^-$) Center-of-Mass system, respectively. To avoid confusion with the lab angles, we will in this section explicitly call these angles θ_{CM} and φ_{CM} .

The details are presented in the following sections.

A. SoLID detector

SoLID with $J\psi$ setup, shown in Fig. 25 will be an all-new detector in Hall A during the 12 GeV era [56]. It is designed to use a solenoid field to sweep away low-energy charged background particles, and can thus carry out experiments using high-energy electron beams

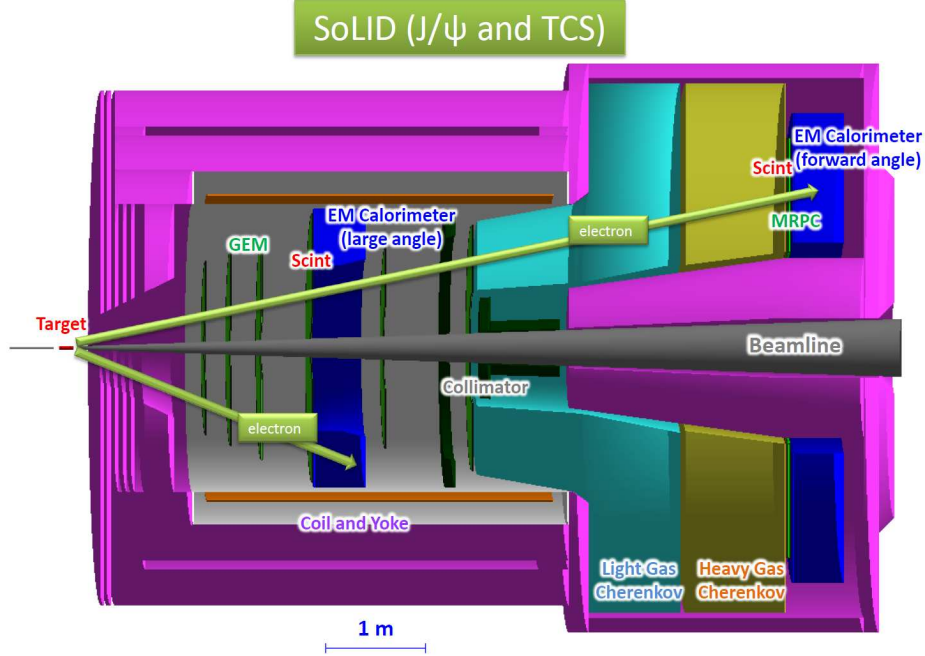


FIG. 25: The SoLID detector with $J\psi$ setup in Hall A.

Parameters	SoLID detector
polar angular range (θ) (target at $z=-315\text{cm}$)	8.5° to 16° for FA and 17° to 24.5° for LA
azimuthal angular range (ϕ)	full
resolution:	
polar angle ($\delta\theta$)	< 0.6 mr
azimuthal angle ($\delta\phi$)	< 5 mr
momentum ($\delta p/p$)	$< 2\%$
PID:	
e/π by EC	full momentum range
e/π by CC	< 4.9 GeV/c at FA
p/K by TOF	< 4.4 GeV/c at FA and < 2 GeV/c at LA

TABLE III: SoLID design characteristics.

incident on unpolarized or polarized targets at luminosities up to $L = 10^{37} \text{ cm}^{-2} \text{ sec}^{-1}$ in an open geometry. It has two groups of the detectors. The forward-angle detectors cover polar angle from 8.5° to 16° and consist of several planes of Gas Electron Multipliers (GEM) for tracking, a light-gas Cherenkov (LGCC) for e/π separation, a heavy gas Cherenkov (HGCC) for π/K separation, a Multi-gap Resistive Plate Chamber (MRPC) for time-of-flight, and an Electromagnetic Calorimeter (FAEC). The large-angle detectors covers polar angle from 17° to

24.5° and consist of several planes of GEM for tracking, an MRPC for time of flight (new for TCS), and an Electromagnetic Calorimeter (LAEC). The design characteristics of SoLID are presented in Table III. Particles in SoLID will be detected and identified by measuring their momenta, time-of-flight, number of photons produced in the threshold Cherenkov counters, and energy losses in the calorimeters and MRPC.

The SoLID solenoid will reuse the CLEO-II magnet. Its superconducting coil and cryo will remain the unchanged. It has a large inner space with a clear bore diameter of 2.9 m and a coil of 3.1 m diameter. The coil length is 3.5 m, with a 3.8 m long cryostat. The coil is made of $5 \times 16 \text{ mm}^2$ aluminum-stabilized superconductor, and runs at 3300 A. Part of the CLEO-II iron flux return will be modified and reused, and two new iron endcaps will be added at the front and back of the solenoid. The axial central field of the solenoidal magnet can reach about 1.4 T.

Six layers of GEM detectors will be used for tracking, providing information on the momentum, angle, and interaction vertex of the detected particles. They will be placed uniformly inside the solenoid magnet. For the forward angle detectors, five layers except for the first layer of GEM detectors will be used. In principle, three points are needed to reconstruct the kinematic variables. The fourth and fifth points will bring enough redundancy to compensate for the inefficiency of the GEM tracking detector. For the large-angle detectors, four layers of GEMs detector except the last two layers will be used. In this case, four layers are enough since the background level at large angles is expected to be smaller. SoLID GEMs will provide full azimuthal angular coverage by using trapezoidal-shaped sectors. The area of a single sector can be as large as $100 \text{ cm} \times 40 \text{ cm}$. Recent advancements in technology, like single-mask GEM etching and GEM splicing, makes it possible to fabricate GEM foils up to $100 \text{ cm} \times 200 \text{ cm}$. The GEM readout is by 2D strips and APV-25 based chips from the funded Scalable Readout System (SRS) project by the CERN RD-51 collaboration.

The Cherenkov detectors (CC) at forward angles have two parts. The light-gas one uses a standard CO_2 gas radiator and can provide e/π separation up to momenta of 4.9 GeV/c with pion rejection in order of 10^3 . The heavy-gas one uses C_4F_8O gas at 1.5 atm and gives a momentum threshold of 2.2 GeV/c and 7.5 GeV/c for pions and kaons, respectively. In both cases, the Cherenkov light is directed by the mirror systems onto Multi-Anode PMTs (MAPMTs) for readout. The MAPMTs have been tested to work with longitudinal magnetic fields up to 400 G.

There is one electromagnetic calorimeter at forward angles and one at large angles. They are made with identical Shashlyk-type modules. Each module is made of a pre-shower and a shower part. The pre-shower detector is simply a 2 radiation-length lead layer and a 2 cm thick scintillator with embedded wave-length-shifting (WLS) fibers for readout. The shower detector is of Shashlyk type, consisting of about 200 layers of 0.5 mm lead and 1.5 mm scintillator, and

many WLS fibers penetrating all layers with a density about $1/\text{cm}^2$ for readout at the back of a module. This type of design can reach a pion rejection factor of more than 100, with good electron efficiency. Its radiation hardness is in the order of 500 krad, which satisfies the high-luminosity condition in SoLID.

MRPC-based time-of-flight systems have recently been used in the RHIC STAR and LHC ALICE experiments, providing a typical time resolution close to 100 ps. With readout strips, it can work inside a magnetic field. Using low-resistive glass, it can gain even an higher rate capability. SoLID experiments have a forward-angle MRPC as part of the planned baseline equipment.

Scintillator pad detector (SPD) will be placed at both forward and large angle. FASPD will provide combined photon rejection with MRPC, but TOF will rely on MRPC for its better time resolution of 100 ps. LASPD will provide both photon rejection and TOF with time resolution of 150 ps.

B. Detection of exclusive e^+e^-p events

The simulations of the SoLID detector for the proposed measurements used an 11 GeV electron beam and a 15 cm long liquid hydrogen target. Exclusive e^+e^-p events, with invariant masses of the lepton pairs in the resonance-free region between 2 and 3 GeV, were generated over a wide range of kinematics by using the standalone event generator genTCS [57]. Both quasi-real photons from electron scattering, according to the equivalent photon approximation (EPA) [58], and real photons from Bremsstrahlung [59] on the target were included. (The former is dominant in the configuration of this experiment.) Each event was weighted by the Bethe-Heitler (BH) cross section from Ref. [9]. The response of the detector was simulated using the SoLID simulation package SoLID GEMC [60].

SoLID does electron and positron identification by combining CC and EC information at the forward angles, and uses only the EC at the large angles. The CC can offline provide a single-pion rejection factor of about 1000, and the EC can do a factor of 100. To suppress the large (0.1 mb) background from two-pion photoproduction, we require that at least one lepton is detected within the CC acceptance at forward angles and has momentum less than 4.9 GeV, which is the SoLID light-gas Cherenkov e/π separation threshold. This will ensure a pion-pair rejection factor of at least 10^7 , which is sufficient to cleanly separate out the lepton-pair events from the pion background. Fig. 26 shows the momentum- and angular distribution of two leptons detected in SoLID. The events with both leptons going into the large-angle detectors are discarded, and a momentum cut at 4.9 GeV is applied for the leptons going to the forward angles.

Protons are mainly identified in SoLID by time-of-flight using the MRPC at forward angle

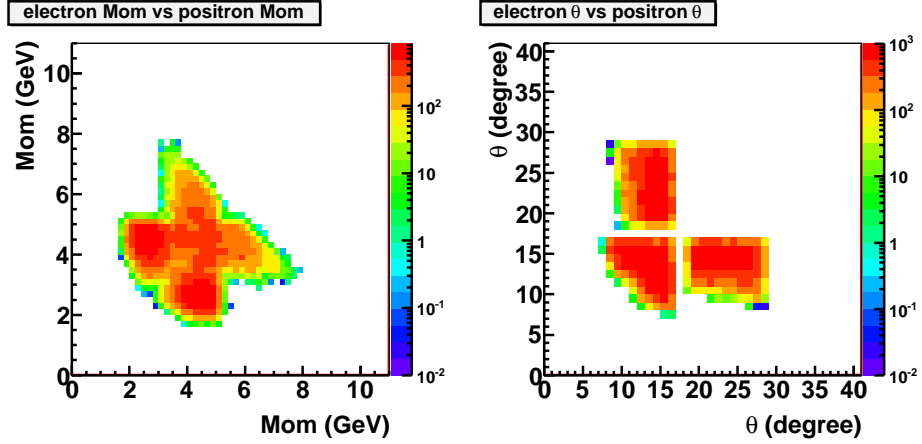


FIG. 26: Decay lepton pair detected by CC and EC *Left panel:* Electron momentum versus positron momentum. *Right panel:* Electron polar angle versus positron polar angle.

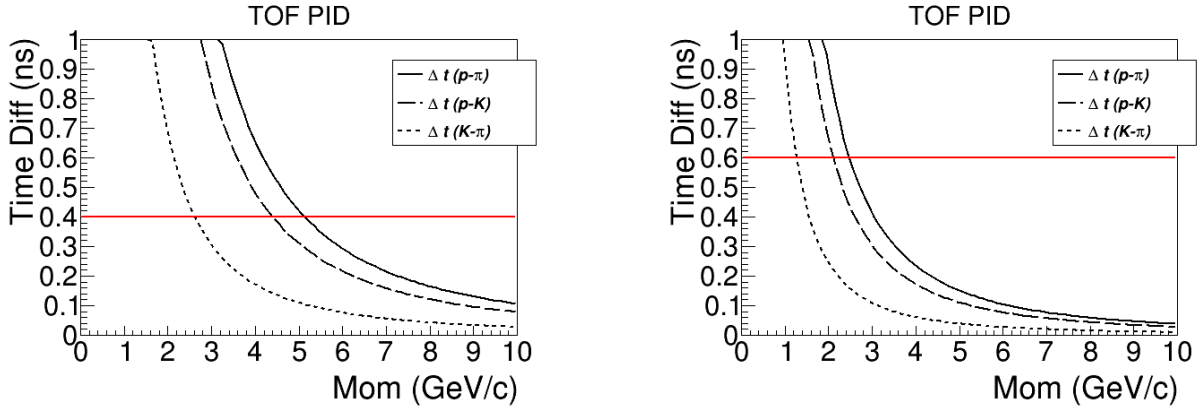


FIG. 27: Proton PID by TOF in the MRPC. The graphs show the time difference vs. momentum for kaons and pions, protons and kaons, and protons and pions for the forward angles (*left panel:*) and the large angles (*right panel:*). The horizontal lines shows where a 4σ separation with time resolution of 100 ps for FA and 150 ps for LA are. The intersecting point of the horizontal line with the protons and kaons time difference line determines the max momentum of proton identification.

with time resolution 100 ps and SPD at large angle with time resolution 150 ps. The flight path of about 750 cm for forward angles and 250 cm for large angles, protons with momenta up to 4.4 GeV and 2 GeV, respectively, can be identified with 4σ separation, as shown in Fig. 27. This allows access to a wide range in t .

Fig. 28 shows the momentum and polar angle distribution of e^+ , e^- , p' , and the photon

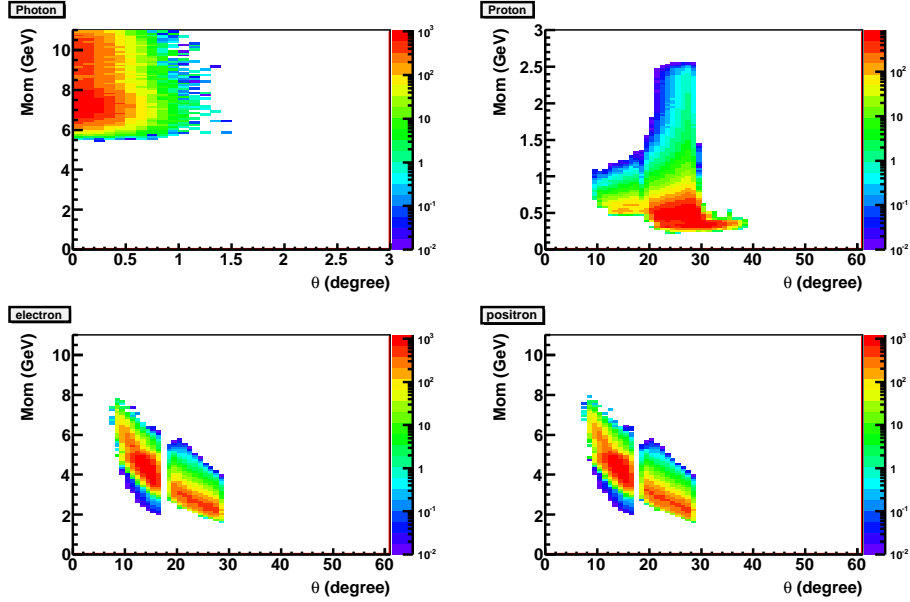


FIG. 28: Momentum and polar angle distribution of the photon, recoil proton, decay electron, and decay positron

from the simulated BH events with invariant mass of lepton pairs $2 \text{ GeV} \leq \sqrt{Q^2} \leq 3 \text{ GeV}$. The decay lepton has momentum from 2 to 8 GeV. The recoil protons mostly have momenta below 2 GeV/c. The photon is reconstructed from the detected lepton pair and proton. Its momentum and angle distribution is affected by detector resolution while reconstructing the other three particles.

To ensure exclusivity of the reaction, cuts need to be applied on the missing particle kinematics. The missing particle can be a very forward scattered electron in quasi-real electroproduction, or an electron that radiated a real photon in photoproduction. In the latter case, the Q^2 is identically zero, and in the former it is kept close to zero. In the simulation, the detected e^+e^-p momenta and angles were smeared by the SoLID detector resolution, thus creating a realistic distribution of kinematic variables for the missing particle. Instead of applying cuts on the transverse momentum, a corresponding cut of $Q^2 < 0.05 \text{ GeV}^2$ was applied. Fig. 29 shows the kinematic variables of the missing particle before and after the cut. As can be seen, the SoLID momentum- and angular resolution is sufficient for cleanly identifying exclusive events with quasi-real photons.

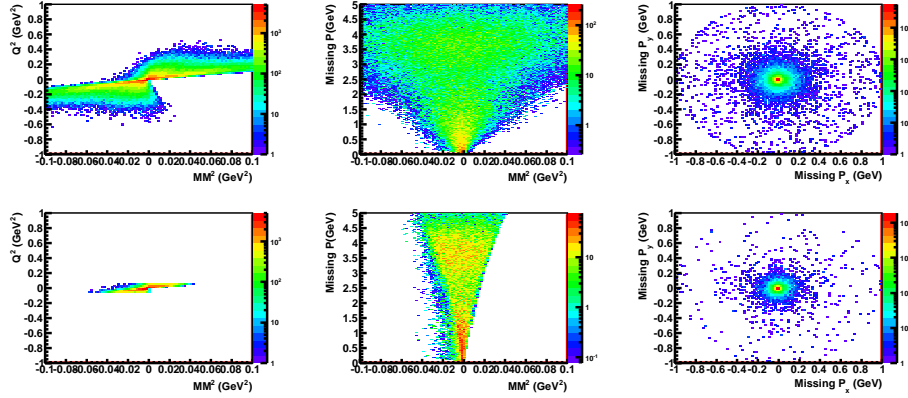


FIG. 29: Missing-particle kinematics before and after the cut $Q^2 < 0.05 \text{ GeV}^2$ *Left panels:* Q^2 versus missing mass squared MM^2 . *Middle panels:* Missing momentum versus missing mass squared MM^2 . *Right panels:* Missing momentum P_x versus missing momentum P_y . *Top row:* before the Q^2 cut *Bottom row:* after the Q^2 cut.

C. Trigger

The approved SoLID J/ψ experiment E12-12-006 [2] has same final state particles like BH and TCS reaction, except the scattered electron. The trigger for the SoLID J/ψ experiment will be the coincidence between two electron kind of signal to ensure the detection of the decay electron and positron from J/ψ .

In Fig. 30, the momentum and angle distribution of all 4 final state particles of the SoLID J/ψ experiment are shown with the condition only decay electron and positron are detected. Its single electron trigger on EC depends on the radius of particles hits to make sure to accept the decay electron or positron. Then additional trigger from the light gas Cherenkov is added to help reject charge pions. MPPC and SPD triggers are also added to reject photon from neutron pions. Finally two single electron triggers are selected within 30 ns time window to form the level 1 trigger.

Comparing Fig. 30 to Fig. 28, the decay pair distribution are very similar between J/ψ and TCS, except TCS needs the trigger threshold to be a little lower. We have carefully select EC trigger threshold varying between 4 GeV to 2 GeV from inner to outer radius. Then we studied the trigger rate considering all possible random background, similar to the study done for SoLID SIDIS He3 in SoLID pCDR [56]. The trigger rate is estimated to be around 40 kHz which is below 100 kHz DAQ limit. Therefore, TCS has no problem to be a run group experiment with J/ψ experiment.

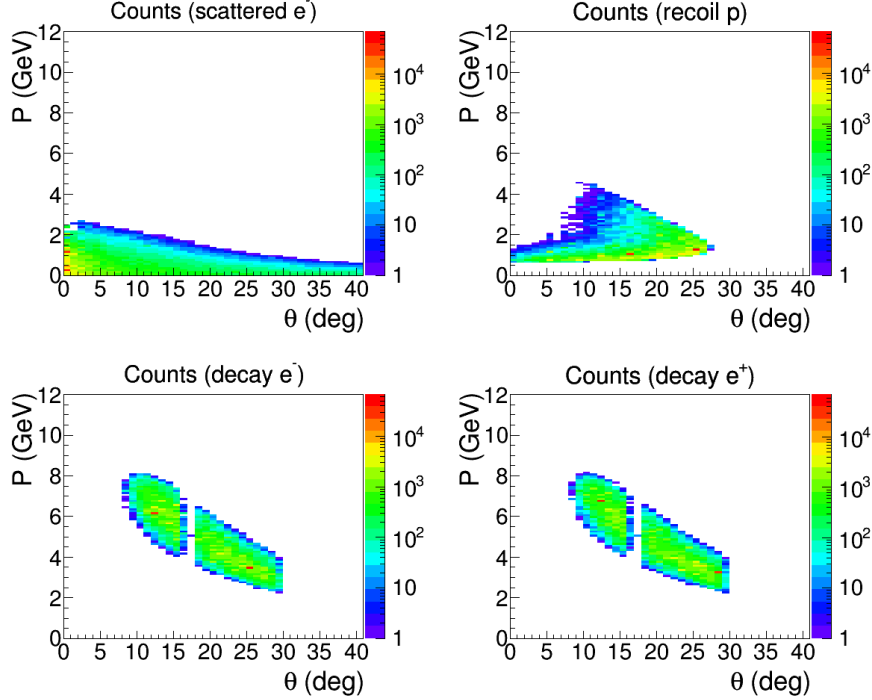


FIG. 30: Momentum and polar angle distribution of the scattered electron, recoil proton, decay electron, and decay positron of SoLID J/ψ experiment with only decay electron and decay positron detected

D. Event Distribution

The simulated data are binned in three kinematic variables: the virtuality of the final-state photon $Q'^2 = M_{e^+e^-}^2$, the four-momentum transfer to the nucleon t , and the skewness of the reaction η . The angular distribution of the decay-lepton pair is evaluated in each bin, for instance as a moment of the weighted cross section, using the lepton center-of-mass angles shown in Fig. 3.

The resulting event distributions illustrating the SoLID acceptance, are shown in Figs. 31 through 34. The first two figures show the acceptance in six bins of η , and the last two in three bins of Q'^2 . The former binning is suited for measuring the Q'^2 -dependence in narrow bins of η to study factorization and higher-twist effects, while the latter would be better for looking at the η -dependence in wider bins of Q'^2 in order to understand the impact of NLO corrections.

Fig. 31 shows how the accessible range in Q'^2 grows at higher values of η . It also shows how the $|t|$ -coverage shifts to higher values as η increases. In actual analysis, the Q'^2 -dependence will also be investigated in wide η bins. The widths of the six bins shown have been chosen to equalize statistics in the range $0.1 < \eta < 0.4$ that can be covered in SoLID. Fig. 32 shows the event distributions in the θ_{CM} vs. φ_{CM} plane for the same six bins in η . The shape of

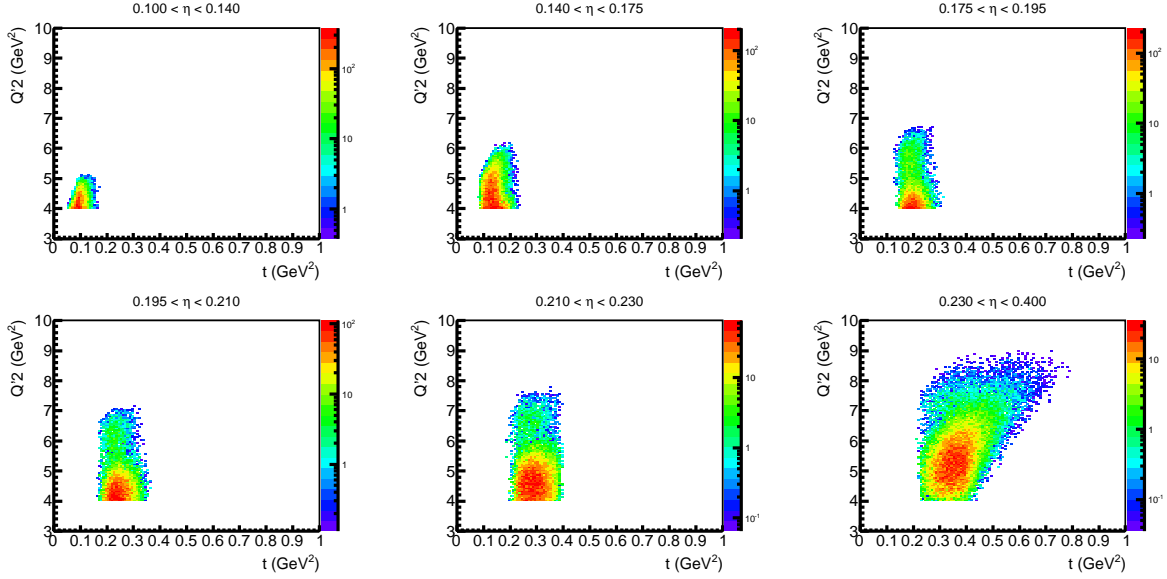


FIG. 31: BH event distribution, in TCS kinematics, showing the SoLID acceptance for exclusive e^+e^-p production and showing the accessible range in Q'^2 and $|t|$ for six bins of η .

the acceptance in the lepton CM-angles is governed by three factors: the “hole” in the forward detector around the beam line, the limit of the large-angle acceptance, and the gap between the large-angle and forward-angle detectors in SoLID. The first two define the general overall shape of the distribution, while the gap leads to a depletion of events in the middle of the band.

Once the Q'^2 -scaling is understood, neither a study of NLO corrections through the η -dependence, nor global fits to the cross section or beam spin asymmetry will require narrow bins in Q'^2 . Fig. 33 shows the distribution of events in η and $|t|$ in two bins of Q'^2 . Fig. 34 shows the corresponding distributions in the θ_{CM} vs. φ_{CM} plane.

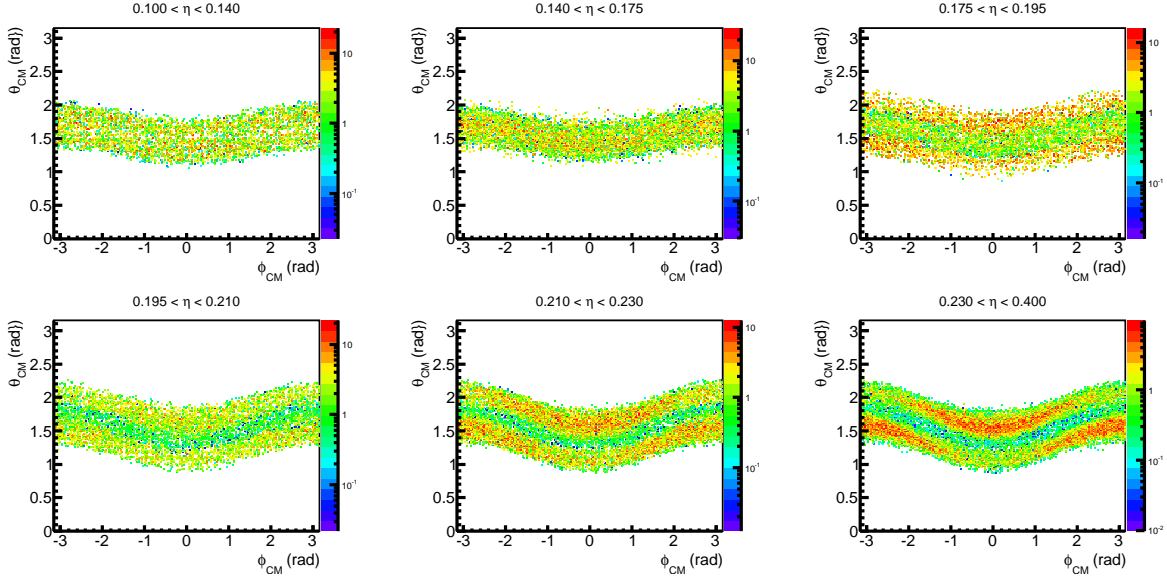


FIG. 32: BH event distribution, in TCS kinematics, showing the SoLID acceptance for exclusive e^+e^-p production and showing the accessible range in θ_{CM} and φ_{CM} for six bins of η .

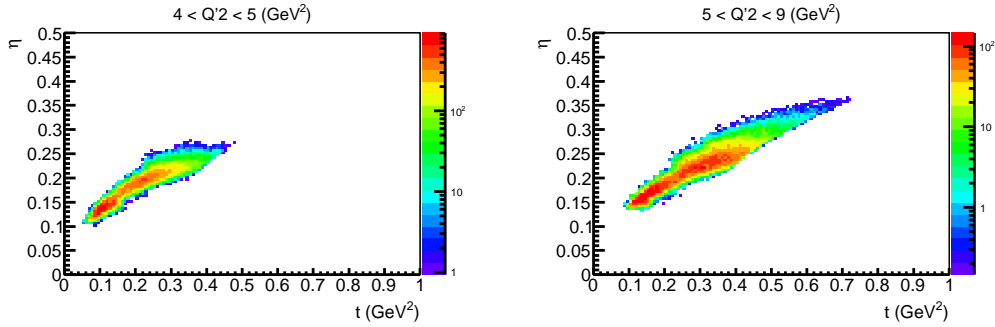


FIG. 33: BH event distribution, in TCS kinematics, showing the SoLID acceptance for exclusive e^+e^-p production and showing the accessible range in η and $|t|$ for two bins in Q^2 .

4. PROJECTED RESULTS

In this section we describe the kinematics and projected uncertainties. The projections have been made for 50 days of running with a luminosity of $10^{37} \text{ cm}^{-2}\text{s}^{-1}$ on a 15 cm long liquid hydrogen target. Only statistical uncertainties are shown.

The results from the TCS analysis will come in the form of the measured differential cross section, beam spin asymmetry, as well as cosine and sine moments of the weighted cross section. The cross section measurement will constrain fits of Compton form factors (CFFs). The cosine and sine moments are also directly related to the helicity amplitudes (and hence CFFs and

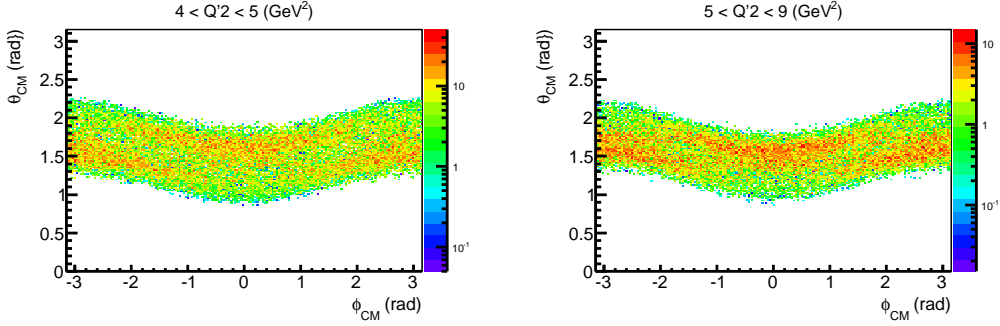


FIG. 34: BH event distribution, in TCS kinematics, showing the SoLID acceptance for exclusive e^+e^-p production and showing the accessible range θ_{CM} and φ_{CM} for the bins of Q'^2 .

GPDs). A comparison of the moments, evaluated within the SoLID acceptance, imposes strong constraints on GPD models.

There are two ways of evaluating the experimental sensitivity of the proposed measurement: through a fit using the VGG approach, or through a comparison of the moments of the weighted cross section with predictions using various GPD models. Both are illustrative in their own way. We will describe both as below.

A. Moment approach

The cosine moment R' , related to $\Re e \tilde{M}^{--}$, sensitive to the real part of the amplitude, will serve as an example of the moment approach. In the extraction of the moments, the angles φ_{CM} and θ_{CM} are integrated over, and only the kinematic variables Q'^2 , η , and $|t|$ remain (refer to The event distribution discussed in Sect. 3 D).

The moment R' differs from the unprimed expression defined in Eqs. (14) and (15) in that the latter is first integrated over θ_{CM} and then independently over φ_{CM} , whereas the primed moment is instead integrated over a band in the θ_{CM} vs. φ_{CM} plane defined through a φ_{CM} -symmetric acceptance function $a(\theta_{CM}, \varphi_{CM})$. This function is chosen such that it coincides with the envelope of the SoLID acceptance for each bin. Using this approach for calculating the theoretical moments allows for a direct and consistent comparison with the moments evaluated from the experimental data. The absolute value of R' can differ somewhat from that of R due to a non-zero BH contribution. An example of this was shown in Fig. 10. However, this does not reduce its sensitivity to $\Re e \tilde{M}^{--}$ or GPD model predictions since the BH contribution can be calculated exactly. And if one wishes to do so, the difference between R and R' can be made very small by adjusting the integration contour slightly, cutting away a small fraction of events along the edges in each bin (BH can be zero even if the contour is not a box).

Still, while the SoLID acceptance does not influence the comparison between data and

theory at the level of the contour of integration in the θ_{CM} vs. φ_{CM} plane, the experimental yields have to be corrected for acceptance, primarily associated with the gap between the inner and outer parts of the detector. This correction is done through simulations, for which the standard SoLID GEMC package will be used. The fact that a similar measurement will also be performed in CLAS12, where different gaps in the acceptance are caused by the six coils of the toroidal magnet, will greatly strengthen the confidence in the acceptance corrections and potentially reduce the systematic uncertainties.

The projected statistical uncertainties for R' are shown in Fig. 35 as a function of Q'^2 for six bins in η . The curves correspond to leading-order (LO), leading-twist calculations using two GPD models, the dual parametrization [16–19] (top curve with blue solid line) and the double distribution [20] with D -term (middle curve with dash-dotted red line) and without D -term (bottom curve with dashed red line). The D -term can also be calculated within the framework of the dual parametrization, but it does not appear as an independent quantity that can easily be varied, hence only one curve is shown. All points use 0.2 GeV^2 wide bins in $|t|$ close to $t = t_{min}$. This shifts $|t|$ towards larger values in the higher η bins, as shown in Fig. 31. The calculation with the dual parametrization has a proper Q'^2 evolution, while the one with the double distribution only has forward evolution, where the forward PDFs are evaluated and then “skewed” to produce the GPDs at a given value of Q'^2 .

The same LO calculations can be applied to the η -dependence. The result is shown in Fig. 36, where we see R' as function of η for two bins in Q'^2 , in 0.2 GeV^2 wide bins in $|t|$ close to $t = t_{min}$. The relation between $|t|$ and η coverage can be seen in Fig. 33. As in Fig. 35, the top curve (solid blue line) corresponds to the dual parametrization, and the middle (dash-dotted red line) and lower (dashed red line) curves to the double distribution with and without D -term, respectively. Here, the large difference between the two models reflects the assumed dependencies of the real part of GPD H on τ (the equivalent of Bjorken x) that are shown in Fig. 6, and to which the cosine moment R' is sensitive.

Fig. 37 shows the projections based on the NLO calculations described in Sect. 2 E. Since the calculations in the figure were made for $Q'^2 = 4 \text{ GeV}^2$, the results are only shown for one, bin in Q'^2 between 4 and 6 GeV^2 . Here, each point corresponds to a 0.3 GeV^2 wide bin in $|t|$. The calculation was done using two GPD models: Goloskokov-Kroll (GK) [45–48] and MSTW, a simple factorizing ansatz for the t -dependence [9] with MSTW08 PDFs [49]. Both LO and NLO results are shown. It is interesting to note that there is a relatively model-independent trend in the calculations. The two upper curves (dashed lines) are both NLO predictions, while the lower two (solid lines) are the LO ones. It seems that for both models the NLO corrections shift R' towards more positive values, but the slope does not change much, and hence the separation between the LO and NLO curves stays about the same for all values of η between 0.1 and 0.3 (going below η of 0.1 the separation in R' does increase, but this is outside of JLab 12 GeV

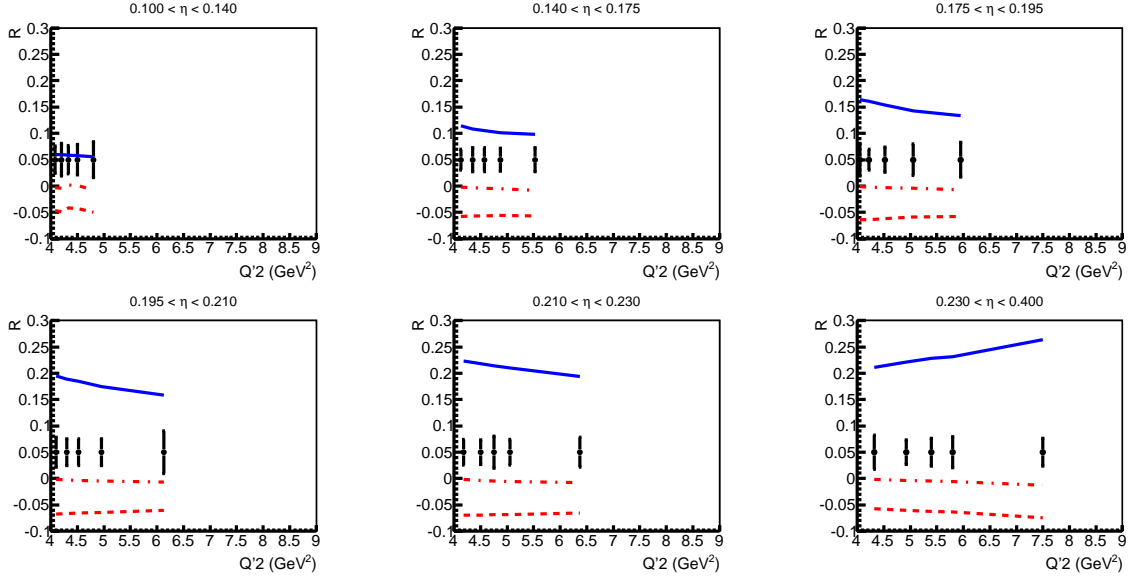


FIG. 35: The cosine moment of the weighted cross section, R' , shown as function of Q'^2 for six bins in η , in 0.2 GeV^2 wide bins in $|t|$ close to $t = t_{min}$. The curves correspond to leading-order, leading-twist calculations using two GPD models, the dual parametrization [16–19] (top, solid blue curve) and the double distribution [20] with D -term (middle, dash-dotted red curve) and without D -term (bottom, dashed red curve). The error bars on the points correspond to 50 days of running. The points are arbitrarily placed at $R' = 0.05$.

kinematics). The GK model prediction (blue curves) for R' is consistently somewhat higher than MSTW (red curves) for both LO and NLO, but this difference is small compared with the overall shift due to the NLO corrections. The model-independence mirrors the discussion in Sect. 2 E where, for instance, Fig. 15 suggests that the general features of the NLO calculations do not strongly depend on the choice of model. That said, it is worth keeping in mind that the GK model is based on \tilde{H} and H , while MSTW only incorporates H , so the predictions shown assume that other contributions are small. It is hoped that Q'^2 evolution will be incorporated into the NLO calculation in the near future, which would allow for reliable projections also at higher values of Q'^2 .

B. Local fit of Compton form factors approach

In this section, we present a projection for the results of the local Compton form factor (CFF) fit method introduced in section 2 F. Instead of generic values for the uncertainties such as 5% and 15% as was taken in section 2 F, we use here more realistic uncertainties, using a luminosity of $10^{37} \text{ cm}^{-2}\text{s}^{-1}$, the SOLID acceptance and a dedicated binning. The cross section

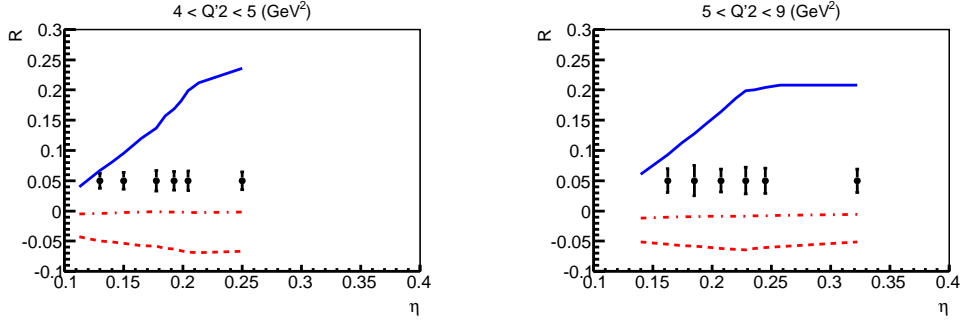


FIG. 36: The cosine moment of the weighted cross section, R' , shown as function of η for two bins in Q'^2 , in 0.2 GeV^2 wide bins in $|t|$ close to $t = t_{min}$. The curves correspond to leading-order, leading-twist calculations using two GPD models, the dual parametrization [16–19] (top, solid blue curve) and the double distribution [20] with D -term (middle, dash-dotted red curve) and without D -term (bottom, dashed red curve). The error bars on the points correspond to 50 days of running. The points are arbitrarily placed at $R' = 0.05$.

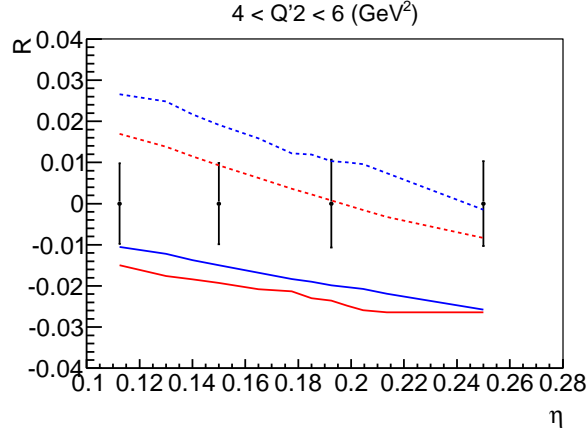


FIG. 37: The cosine moment of the weighted cross section, R' , shown as function of η for in a bin of Q'^2 from 4 to 6 GeV^2 and a 0.3 GeV^2 wide bin of $|t|$. The upper (dotted) curves are the NLO predictions, while the (solid) lower pair are the LO ones. Within each pair, the upper (blue) curve was calculated using the GK model and the lower (red) one using MSTW. The error bars on the points correspond to 50 days of running. The points are arbitrarily placed at $R' = 0$.

used for the counting rates is based on the calculations of Ref. [37]. For the binning, we take two-dimensional (η, Q'^2) bins, t bins and ϕ_{CM} bins (from 0° to 360°), as presented in Fig. 38 and table IV. We recall that CFFs depend only on η and t and that the method consists in fitting, at given (η, t) values, the ϕ_{CM} distribution of TCS observables so as to extract (some of) the CFFs: $Re\{\mathcal{H}\}$, $Re\{\mathcal{E}\}$, $Re\{\tilde{\mathcal{H}}\}$, $Re\{\tilde{\mathcal{E}}\}$, $Im\{\mathcal{H}\}$, $Im\{\mathcal{E}\}$, $Im\{\tilde{\mathcal{H}}\}$ and $Im\{\tilde{\mathcal{E}}\}$. In the following, the distributions will therefore be integrated over $\theta \in [45^\circ, 135^\circ]$. In the context of

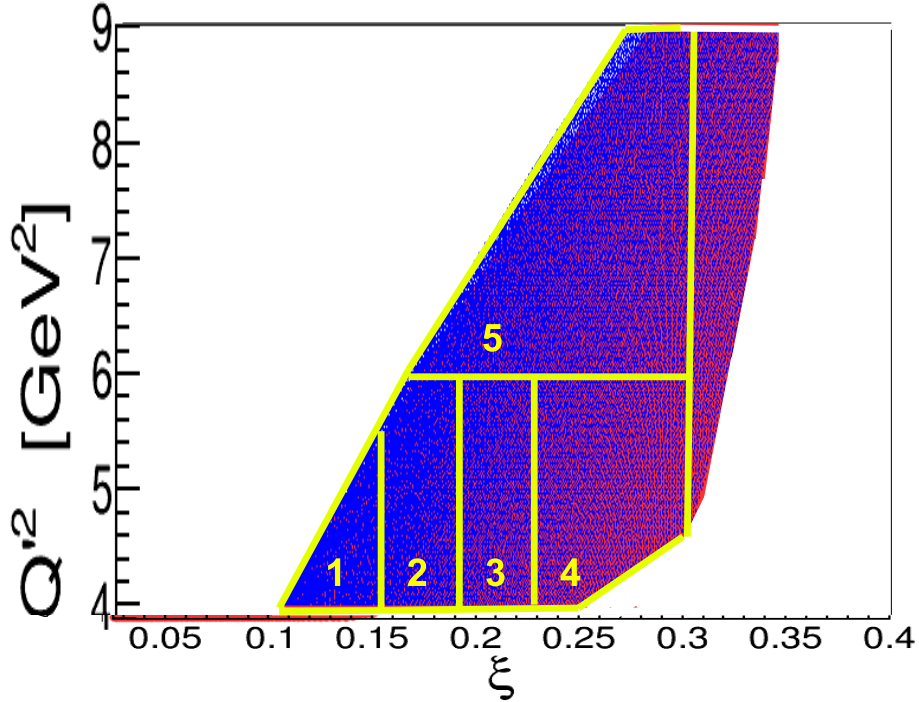


FIG. 38: Phase space for TCS as a function of Q^2 and $\xi(\eta)$ with the binning definition for Hall A SoLID data.

this proposal, the observables will be the unpolarized cross section σ and the spin asymmetry obtained with a circularly polarized photon beam $\Delta\sigma_{LU}$. As outlined in section 2 F, with these observables, we expect to extract and be particularly sensitive to the $Re\{\mathcal{H}\}$ and $Im\{\mathcal{H}\}$ CFFs, which are the dominant contributions.

N	$\xi(\eta)$ limits	Q^2 limits (GeV ²)	-t limits (GeV ²)
1.	0.10, 0.15	4, 6	[0.1, 0.2],[0.2, 0.5]
2.	0.15, 0.19	4, 6	[0.1, 0.2],[0.2, 0.5],[0.5, 1]
3.	0.19, 0.23	4, 6	[0.2, 0.5],[0.5, 1]
4.	0.23, 0.30	4, 6	[0.2, 0.5],[0.5, 1]
5.	0.15, 0.30	6, 9	[0.2, 0.5],[0.5, 1]

TABLE IV: Proposed binning for TCS analysis in Hall A. The given values are the edges of the bins.

Under the SoLID TCS running condition outlined above, we show in Fig. 39 an example of the expected number of counts for the ϕ_{CM} distributions of the 3rd (η, Q^2) bin and its associated t bins. For our CFF fits, to the statistical errors deduced from such distributions, we choose to add a 6% systematic error.

Since the idea is to fit simultaneously TCS and DVCS data as presented in section 2 F,

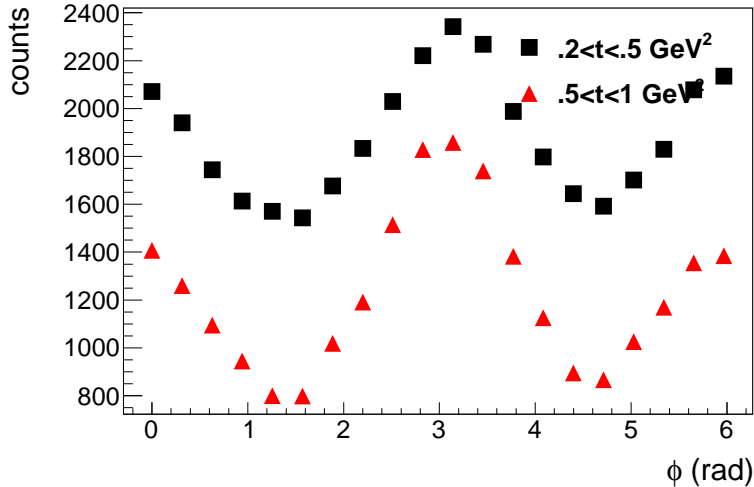


FIG. 39: Expected counting rates for TCS in the SoLID acceptance as a function of ϕ_{cm} for the 3rd (η, Q^2) bin and for its associated t bins given in table IV.

we choose a (η, t) bin which is accessible to both TCS and DVCS. We recall that DVCS is currently being measured in Hall A with an 11 GeV beam (E12-06-114). We show in table V the result of the CFF fit, fitting simultaneously the ϕ_{CM} and Φ_{LH} distributions of the σ and $\Delta\sigma_{LU}$ observables of TCS and DVCS, i.e. 4 observables in all. Our results for the two dominant CFFs $Re\{\mathcal{H}\}$ and $Im\{\mathcal{H}\}$ CFFs which come out of fit, are presented in table V for the particular bin $(\eta = 0.185, -t = 0.3 \text{ GeV}^2)$, with $Q'^2 = 5 \text{ GeV}^2$ for TCS and $Q^2 = 2.5 \text{ GeV}^2$ for DVCS. These more realistic and precise numbers of table V essentially confirm the ones of table II, which were obtained under coarse assumptions (global 5% and 15% uncertainties, independent of detector's acceptance, ϕ_{CM} and Φ_{LH} , etc...).

C. Conclusion

In conclusion, the physics of deeply-virtual Compton scattering is a rich topic, and the possibility to study the universality of GPDs and the timelike-spacelike correspondence through TCS will add an important piece to the puzzle. This proposed high-luminosity measurement in SoLID with high-statistics TCS data using a circularly polarized beam will have a significant impact on the extraction of the CFFs. It will allow a combined fit with the DVCS data to constrain the global GPD with reduced uncertainty. Besides, for moments such as the observable R' , the high-statistics of SoLID TCS will allow to study the Q'^2 -dependence and the η -dependence and provide guidance on GPD modeling, such as the magnitude of the D -term and have the potentials to look into NLO effect.

	$(\sigma, \Delta\sigma_{LU})$ DVCS + TCS _e
$\sigma^+(Re\{\mathcal{H}\})$	+82%
$\sigma^-(Re\{\mathcal{H}\})$	-77%
$\sigma^+(Im\{\mathcal{H}\})$	+16%
$\sigma^-(Im\{\mathcal{H}\})$	-40%

TABLE V: The table shows the uncertainties on the extracted $Im\{\mathcal{H}\}$ and $Re\{\mathcal{H}\}$ CFFs (which are the dominant contributors to the fitted observables) obtained with our simulations. Like in table II, we list the positive σ^+ and negative σ^- errors. We recall that, the fit being under-constrained (eight free parameters for only 4 observables to be fitted), the problem is not linear and the errors are asymmetric. The observables fitted simultaneously by the same CFFs are σ (the unpolarized cross section) and $\Delta\sigma_{LU}$ (the beam polarized cross section; with electrons for DVCS and photons for TCS).

5. SYSTEMATIC UNCERTAINTIES

The two main sources of systematic uncertainty for the proposed measurement are acceptance corrections and lepton identification. The former can be expected to be comparable to estimates for cross section measurements with CLAS12, *i.e.*, to be at least of the order of 5%. As discussed in Sec. 3D, the acceptance studies will be performed through SoLID simulations and reconstruction.

As described in Sec. 3B, lepton identification will be performed using the Cherenkov counters (CC) and the electromagnetic calorimeters (EC). All events used for the analysis of this proposed experiment will have both leptons detected in one of the ECs, and at least within the (angular and momentum) acceptance of the CCs. For those pairs, the two-pion rejection factor is expected to be at about 10^7 . The remaining pairs will be discarded from the analysis. This will not have any significant impact on the statistical uncertainty.

In the photon-energy range of the proposed experiment, the total cross section for $\pi^+\pi^-$ production is 0.1 mb. With a pion pair rejection factor of 10^7 , there would be a pion background at the 5% level if the total e^+e^- cross section was 0.1 nb. This is comparable to the J/ψ cross section in JLab 12 GeV kinematics. The BH cross section integrated over $0.5 < Q'^2 < 7$ GeV² at $E_\gamma = 11$ GeV is 34 nb. For most kinematics, and in particular those in the primary range of interest (*i.e.*, for $4 < Q'^2 < 9$ GeV²), the contribution to the total uncertainty from lepton pair misidentification should be small compared with the statistical uncertainty, and the systematic uncertainty in the acceptance correction. Performing the measurement with two independent setups, SoLID and CLAS12, will greatly increase our confidence in being able to correctly estimate the systematic uncertainties, and in particular those related to acceptance.

6. RUNNING CONDITION

This proposed experiment will require a longitudinally polarized ($> 80\%$) 11 GeV beam and an unpolarized proton target in the SoLID detector. For photoproduction using quasi-real photons, the detector will need a recoil baryon detection and identification capability. Furthermore, specifically for e^+e^- photoproduction, the trigger has to be set up for a coincidence of two leptons, with the additional condition that at least one of them produces a signal in the Cherenkov. The running condition and trigger setting are exactly same as the approved SoLID J/ψ experiment E12-12-006 [2]. During the SoLID J/ψ approved beam-time of 50 days for production and 10 days for calibration, TCS data will be collected at the same time, thus work as a run group experiment.

-
- [1] JLab experiment E12-12-001: Timelike Compton Scattering and J/ψ photoproduction on the proton in e^+e^- pair production with CLAS12 at 11 GeV.
http://www.jlab.org/exp_prog/proposals/12/PR12-12-001.pdf.
- [2] JLab experiment E12-12-006: Near Threshold Electroproduction of J/ψ at 11 GeV.
http://www.jlab.org/exp_prog/proposals/12/PR12-12-006.pdf.
- [3] K. Goeke, M.V. Polyakov, and M. Vanderhaeghen. Hard exclusive reactions and the structure of hadrons. *Progress in Particle and Nuclear Physics*, 47(2):401 – 515, 2001, hep-ph/0106012.
- [4] M. Diehl. Generalized parton distributions. *Physics Reports*, 388(24):41 – 277, 2003, hep-ph/0307382.
- [5] A.V. Belitsky and A.V. Radyushkin. Unraveling hadron structure with generalized parton distributions. *Physics Reports*, 418(16):1 – 387, 2005, hep-ph/0504030.
- [6] John C. Collins, Leonid Frankfurt, and Mark Strikman. Factorization for hard exclusive electroproduction of mesons in QCD. *Phys. Rev. D*, 56:2982–3006, Sep 1997, hep-ph/9611433.
- [7] John C. Collins and Andreas Freund. Proof of factorization for deeply virtual compton scattering in QCD. *Phys. Rev. D*, 59:074009, Feb 1999, hep-ph/9801262.
- [8] Xiangdong Ji. Gauge-Invariant Decomposition of Nucleon Spin. *Phys. Rev. Lett.*, 78:610–613, Jan 1997, hep-ph/9603249.
- [9] E.R. Berger, M. Diehl, and B. Pire. Timelike Compton scattering: exclusive photoproduction of lepton pairs. *The European Physical Journal C - Particles and Fields*, 23:675–689, 2002, hep-ph/0110062.
- [10] Michel Guidal, Herve Moutarde, and Marc Vanderhaeghen. Generalized Parton Distributions in the valence region from Deeply Virtual Compton Scattering. 2013, 1303.6600.
- [11] M. Guidal. A Fitter code for Deep Virtual Compton Scattering and Generalized Parton Distributions. *Eur. Phys. J.*, A37:319–332, 2008, arXiv:0807.2355 [hep-ph].
- [12] V.M. Braun and A.N. Manashov. Kinematic power corrections in off-forward hard reactions. *Phys.Rev.Lett.*, 107:202001, 2011, 1108.2394.
- [13] V.M. Braun, A.N. Manashov, and B. Pirnay. Finite- t and target mass corrections to deeply virtual Compton scattering. *Phys.Rev.Lett.*, 109:242001, 2012, 1209.2559.
- [14] B. Pire, L. Szymanowski, and J. Wagner. Next-to-leading order corrections to timelike, spacelike, and double deeply virtual Compton scattering. *Phys. Rev. D*, 83:034009, Feb 2011, arXiv:1101.0555 [hep-ph].
- [15] D. Müller, B. Pire, L. Szymanowski, and J. Wagner. On timelike and spacelike hard exclusive reactions. 2012, arXiv:1203.4392 [hep-ph].
- [16] M.V. Polyakov and A.G. Shuvaev. On 'dual' parametrizations of generalized parton distributions. 2002, hep-ph/0207153.
- [17] V. Guzey and T. Teckentrup. The Dual parameterization of the proton generalized parton distribution functions H and E and description of the DVCS cross sections and asymmetries. *Phys. Rev.*, D74:054027, 2006, hep-ph/0607099.
- [18] V. Guzey and T. Teckentrup. On the mistake in the implementation of the minimal model of the dual parameterization and resulting inability to describe the high-energy DVCS data. *Phys. Rev.*,

- D79:017501, 2009, arXiv:0810.3899 [hep-ph].
- [19] Maxim V. Polyakov and Kirill M. Semenov-Tian-Shansky. Dual parametrization of GPDs versus double distribution Ansatz. *Eur. Phys. J.*, A40:181–198, 2009, arXiv:0811.2901 [hep-ph].
 - [20] A.V. Radyushkin. Double distributions and evolution equations. *Phys. Rev.*, D59:014030, 1999, hep-ph/9805342.
 - [21] M. V. Polyakov and C. Weiss. Skewed and double distributions in the pion and the nucleon. *Phys. Rev. D*, 60:114017, Nov 1999, hep-ph/9902451.
 - [22] Andrei V. Belitsky, Dieter Mueller, A. Kirchner, and A. Schafer. Twist three analysis of photon electroproduction off pion. *Phys. Rev.*, D64:116002, 2001, hep-ph/0011314.
 - [23] A.V. Radyushkin. Generalized Parton Distributions and Their Singularities. *Phys. Rev.*, D83:076006, 2011, 1101.2165.
 - [24] R. L. Jaffe and Aneesh Manohar. The G(1) Problem: Fact and Fantasy on the Spin of the Proton. *Nucl. Phys.*, B337:509–546, 1990, [INSPIRE].
 - [25] M. V. Polyakov. Generalized parton distributions and strong forces inside nucleons and nuclei. *Phys. Lett.*, B555:57–62, 2003, hep-ph/0210165.
 - [26] K. Goeke et al. Nucleon form-factors of the energy momentum tensor in the chiral quark-soliton model. *Phys. Rev.*, D75:094021, 2007, hep-ph/0702030.
 - [27] M. Gockeler et al. Generalized parton distributions from lattice QCD. *Phys. Rev. Lett.*, 92:042002, 2004, hep-ph/0304249.
 - [28] I.V. Anikin and O.V. Teryaev. Dispersion relations and subtractions in hard exclusive processes. *Phys. Rev.*, D76:056007, 2007, arXiv:0704.2185 [hep-ph].
 - [29] M. Diehl and D. Yu. Ivanov. Dispersion representations for hard exclusive processes: beyond the Born approximation. *Eur. Phys. J.*, C52:919–932, 2007, arXiv:0707.0351 [hep-ph].
 - [30] M.V. Polyakov. Tomography for amplitudes of hard exclusive processes. *Phys. Lett.*, B659:542–550, 2008, arXiv:0707.2509 [hep-ph].
 - [31] Stanley J. Brodsky, Francis E. Close, and J.F. Gunion. Compton scattering and fixed poles in parton field theoretic models. *Phys. Rev.*, D5:1384, 1972, [INSPIRE].
 - [32] Stanley J. Brodsky, Francis E. Close, and J.F. Gunion. Phenomenology of Photon Processes, Vector Dominance and Crucial Tests for Parton Models. *Phys. Rev.*, D6:177, 1972, [INSPIRE].
 - [33] Stanley J. Brodsky, Francis E. Close, and J.F. Gunion. A gauge - invariant scaling model of current interactions with regge behavior and finite fixed pole sum rules. *Phys. Rev.*, D8:3678, 1973, [INSPIRE].
 - [34] Stanley J. Brodsky, Felipe J. Llanes-Estrada, and Adam P. Szczepaniak. Local Two-Photon Couplings and the J=0 Fixed Pole in Real and Virtual Compton Scattering. *Phys. Rev.*, D79:033012, 2009, arXiv:0812.0395 [hep-ph].
 - [35] B. Pire, L. Szymanowski, and J. Wagner. Can one measure timelike Compton scattering at LHC?. *Phys. Rev. D*, 79:014010, Jan 2009, arXiv:0811.0321 [hep-ph].
 - [36] V. Yu. Petrov et al. Off-forward quark distributions of the nucleon in the large N(c) limit. *Phys. Rev.*, D57:4325–4333, 1998, hep-ph/9710270.
 - [37] Guidal M. Boer M. and Vanderhaeghen M. Single and double polarization observables in timelike compton scattering off proton. arXiv:1501.00270[hep-ph].
 - [38] Boer M. and Guidal M. Generalized parton distributions and deeply virtual compton scattering. *J.*

- Phys. G*, 42:034023, year =.
- [39] Dieter Mueller, B. Pire, L. Szymanowski, and J. Wagner. On timelike and spacelike hard exclusive reactions. *Phys.Rev.*, D86:031502, 2012, 1203.4392.
 - [40] H. Moutarde, B. Pire, F. Sabatie, L. Szymanowski, and J. Wagner. On timelike and spacelike deeply virtual Compton scattering at next to leading order. *Phys.Rev.*, D87:054029, 2013, 1301.3819.
 - [41] Xiang-Dong Ji and Jonathan Osborne. One loop QCD corrections to deeply virtual Compton scattering: The Parton helicity independent case. *Phys.Rev.*, D57:1337–1340, 1998, hep-ph/9707254.
 - [42] L. Mankiewicz, G. Piller, E. Stein, M. Vanttinen, and T. Weigl. NLO corrections to deeply virtual Compton scattering. *Phys.Lett.*, B425:186–192, 1998, hep-ph/9712251.
 - [43] A.V. Belitsky, D. Müller, L. Niedermeier, and A. Schäfer. Deeply virtual Compton scattering in next-to-leading order. *Physics Letters B*, 474(12):163 – 169, 2000, hep-ph/9908337.
 - [44] Andreas Freund and Martin F. McDermott. A Next-to-leading order QCD analysis of deeply virtual Compton scattering amplitudes. *Phys.Rev.*, D65:074008, 2002, hep-ph/0106319.
 - [45] S.V. Goloskokov and P. Kroll. Vector meson electroproduction at small Bjorken-x and generalized parton distributions. *Eur.Phys.J.*, C42:281–301, 2005, hep-ph/0501242.
 - [46] S.V. Goloskokov and P. Kroll. The longitudinal cross section of vector meson electroproduction. *The European Physical Journal C - Particles and Fields*, 50:829–842, 2007, hep-ph/0611290.
 - [47] S.V. Goloskokov and P. Kroll. The Role of the quark and gluon GPDs in hard vector-meson electroproduction. *Eur.Phys.J.*, C53:367–384, 2008, 0708.3569.
 - [48] Peter Kroll, Herve Moutarde, and Franck Sabatie. From hard exclusive meson electroproduction to deeply virtual Compton scattering. *Eur.Phys.J.*, C73:2278, 2013, 1210.6975.
 - [49] A.D. Martin, W.J. Stirling, R.S. Thorne, and G. Watt. Parton distributions for the LHC. *Eur.Phys.J.*, C63:189–285, 2009, 0901.0002.
 - [50] N. Kivel, Maxim V. Polyakov, and M. Vanderhaeghen. DVCS on the nucleon: Study of the twist - three effects. *Phys.Rev.*, D63:114014, 2001, hep-ph/0012136.
 - [51] M. Guidal and H. Moutarde. Generalized Parton Distributions from Deeply Virtual Compton Scattering at HERMES. *The European Physical Journal A - Hadrons and Nuclei*, 42:71–78, 2009, arXiv:0905.1220 [hep-ph].
 - [52] M. Guidal. Generalized parton distributions from deep virtual compton scattering at CLAS. *Physics Letters B*, 689(45):156 – 162, 2010, arXiv:1003.0307 [hep-ph].
 - [53] M. Guidal. Constraints on the generalized parton distribution from deep virtual Compton scattering measured at HERMES. *Physics Letters B*, 693(1):17 – 23, 2010, arXiv:1005.4922 [hep-ph].
 - [54] R. Paremuzyan. *Timelike Compton Scattering*. PhD thesis, Yerevan, 2010.
 - [55] V. Guzey. Code for cross section calculations for Bethe-Heitler and Timelike Compton Scattering.
 - [56] SoLID Preliminary Conceptual Design Report.
http://hallaweb.jlab.org/12GeV/SoLID/download/doc/solid_precdr.pdf.
 - [57] genTCS, an event generator of exclusive Bethe-Heitler (BH) for TCS study.
SoLID software repository: <https://jlabsvn.jlab.org/svnroot/solid/evgen/genTCS>.
 - [58] Paul Kessler. Photon fluxes and the EPA. 1994. <http://lss.fnal.gov/archive/other/lpc-94-35.pdf>.
 - [59] J. Beringer and et al. The Review of Particle Physics. *Phys. Rev. D*, 86:010001, 2012.
 - [60] SoLID GEMC, GEANT4 based simulation package GEMC for SoLID.
GEMC website: <http://gemc.jlab.org>,

SoLID software repository: [https://jlabsvn.jlab.org/svnroot/solid/solid\\$_\\$gemc](https://jlabsvn.jlab.org/svnroot/solid/solid$_$gemc).